

1 A dataset of vertical profiles of O<sub>3</sub> and HONO from the hyperspectral  
2 vertical remote sensing network in China (2021-2024)

3 Tiliang Zou<sup>1,#</sup>, Chengzhi Xing<sup>2,#,\*</sup>, Xiangguang Ji<sup>3,\*</sup>, Shaocong Wei<sup>4</sup>, Wei  
4 Tan<sup>2</sup>, Haoran Liu<sup>3</sup>, Cheng Liu<sup>2,3,5,6,7,\*</sup>

5 <sup>1</sup> School of Environmental Science and Optoelectronic Technology, University of Science and  
6 Technology of China, Hefei 230026, China

7 <sup>2</sup>Key Lab of Environmental Optics & Technology, Anhui Institute of Optics and Fine Mechanics,  
8 Hefei Institutes of Physical Science, Chinese Academy of Sciences, Hefei, 230031, China

9 <sup>3</sup> Institute of Physical Science and Information Technology, Anhui University, Hefei 230601,  
10 China

11 <sup>4</sup>Institute of Environment Hefei Comprehensive National Science Center, Hefei, 230031, China

12 <sup>5</sup> Department of Precision Machinery and Precision Instrumentation, University of Science and  
13 Technology of China, Hefei 230026, China

14 <sup>6</sup> Center for Excellence in Regional Atmospheric Environment, Institute of Urban Environment,  
15 Chinese Academy of Sciences, Xiamen 361021, China

16 <sup>7</sup> Key Laboratory of Precision Scientific Instrumentation of Anhui Higher Education Institutes,  
17 University of Science and Technology of China, Hefei 230026, China

18

19 # These authors contributed equally to this work.

20 \*Corresponding to: Chengzhi Xing ([xingcz@aiofm.ac.cn](mailto:xingcz@aiofm.ac.cn)); Xiangguang Ji ([xgji@ahu.edu.cn](mailto:xgji@ahu.edu.cn));  
21 Cheng Liu ([chliu81@ustc.edu.cn](mailto:chliu81@ustc.edu.cn))

22

## 23 Abstract

24 Photolysis of HONO and O<sub>3</sub> in the troposphere is one of the primary sources of  
25 OH radical and a fundamental control on atmospheric oxidative capacity. Their  
26 vertical distributions and diurnal evolution are therefore essential for elucidating  
27 photochemical processes in the planetary boundary layer and the lower free  
28 troposphere. Yet long-term, continuous observations of the vertical profiles of HONO,  
29 O<sub>3</sub>, their photolysis frequencies, and the resulting OH production rates remain  
30 extremely limited, particularly at multi-regional and interannual scales. Here we  
31 present vertical profile measurements of HONO and O<sub>3</sub> acquired by the Chinese  
32 Hyperspectral Vertical Remote Sensing Network during 2021–2024. The dataset  
33 comprises 22 representative sites spanning urban, suburban, plateau, and basin  
34 environments, covering diverse surface and climatic regimes. Profiles extend from the  
35 surface to 4 km with ~100 m vertical resolution and ~15 min temporal resolution.  
36 Using the TUV model with co-retrieved aerosol and trace-gas profiles, we derive  
37 photolysis frequencies of HONO and O<sub>3</sub> and the corresponding OH production rates,  
38 P(OH)<sub>HONO</sub> and P(OH)<sub>O<sub>3</sub></sub>. The observations reveal robust regional patterns in the  
39 diurnal and vertical structure of tropospheric photochemical activity. Photolysis  
40 frequencies peak near local noon and generally increase with altitude from the surface  
41 layer to the upper mixed layer and the lower free troposphere, whereas OH production  
42 rates reach their maxima within the boundary layer and decrease with height.  
43 Processed using a unified retrieval framework and rigorous quality control, this  
44 dataset provides quantitative constraints on the contribution of HONO and O<sub>3</sub>  
45 photolysis to tropospheric OH, supports improved radical parameterizations in  
46 chemical transport models, and enables synergistic multi-platform remote sensing  
47 analyses. By delivering the first systematic, long-term vertical profiles of HONO, O<sub>3</sub>,  
48 and their OH production in China, this public dataset fills a critical observational gap  
49 and offers a robust basis for investigating the spatiotemporal evolution of tropospheric  
50 oxidative capacity across regions and altitude ranges, with substantial scientific  
51 significance and long-term applicability. The dataset is available for free at Zenodo  
52 (<https://doi.org/10.5281/zenodo.18489836>, Zou et al., 2026)

53

## 54 1. Introduction

55 Over the past decade, “the implementation of China’s Air Pollution Prevention  
56 and Control Action Plan” (2013) and “the Three-Year Action Plan for Defending the  
57 Blue Sky” (2018) has led to a marked reduction in fine particulate matter (PM<sub>2.5</sub>)  
58 nationwide (Liu et al., 2023b; Wang et al., 2020). In contrast, ozone (O<sub>3</sub>)—a  
59 secondary pollutant and a major atmospheric oxidant—has continued to increase on  
60 average in economically developed regions such as the Beijing–Tianjin–Hebei area,  
61 the Yangtze River Delta, and the Pearl River Delta, where it has emerged as the most  
62 intractable air-quality problem after PM<sub>2.5</sub> (Guo et al., 2023; He et al., 2023a; Li et al.,  
63 2020; Lyu et al., 2025; Zou et al., 2025). To address the observational gaps in these  
64 and other key regions, we developed a comprehensive dataset. The dataset comprises

65 measurements from 22 ground-based sites across five major regions of China—North,  
66 East, Southwest, South, and Central China. Photochemical air pollution is a dominant  
67 driver of urban and regional air-quality degradation, characterized by the rapid  
68 sunlight-driven accumulation of secondary species, most notably O<sub>3</sub> (Dewan and  
69 Lakhani, 2022; Donzelli and Suarez-Varela, 2024; Sharma et al., 2025; Wang et al.,  
70 2025b). Beyond being a typical secondary pollutant, O<sub>3</sub> is a powerful oxidant that  
71 exerts substantial impacts on regional climate, ecosystems, and human health (Monks  
72 et al., 2015; Sharma et al., 2025; Wang et al., 2025b; Xing et al., 2017). Nitrous acid  
73 (HONO), a short-lived reactive nitrogen species, occurs at relatively low  
74 concentrations but represents a major primary source of the OH radical, the key  
75 “detergent” of the troposphere (Andersen et al., 2023; He et al., 2023c; Song et al.,  
76 2023a; Zhang et al., 2023a). In polluted environments, photolysis of HONO can  
77 account for 20–80% of total OH production, and its relative importance is particularly  
78 pronounced during early morning and late afternoon, when solar elevation is low and  
79 alternative OH sources are less efficient (Elshorbany et al., 2010; He et al., 2023c;  
80 Zhang et al., 2023a). A quantitative understanding of the formation and transport of  
81 both HONO and O<sub>3</sub> is therefore essential for elucidating the mechanisms of  
82 tropospheric photochemical pollution and for designing effective mitigation strategies.

83 Despite extensive research on HONO and O<sub>3</sub>, major gaps persist in observations  
84 of their vertical structure and in the parameterization of key photochemical processes,  
85 limiting a mechanistic understanding of photochemical air pollution (Liu et al., 2023a;  
86 Wang et al., 2018, 2025c; Zhang et al., 2024; Zhu et al., 2025b). Vertical  
87 measurements remain particularly sparse, and concurrent profiles of HONO and O<sub>3</sub>  
88 are largely unavailable (Garcia-Nieto et al., 2018a; Song et al., 2023a; Wang et al.,  
89 2018, 2025c; Zhu et al., 2025b). China National Environmental Monitoring Center  
90 (CNEMC), with more than 2,000 surface stations, provides routine measurements of  
91 PM<sub>2.5</sub>, NO<sub>2</sub>, and SO<sub>2</sub>, but lacks observations of key photochemical precursors such as  
92 HONO and volatile organic compounds (VOCs) (Liu et al., 2023a; Qu et al., 2020;  
93 Zhang et al., 2024; Zhu et al., 2025b). More fundamentally, surface observations  
94 alone cannot resolve pollutant distributions within the planetary boundary layer or  
95 capture variations in vertical atmospheric structure (Wang et al., 2018, 2019, 2025c;  
96 Xuan et al., 2025a; Zhu et al., 2025b), and exclusive reliance on near-surface data  
97 may therefore bias assessments of regional transport and accumulation (Liu et al.,  
98 2023a; Wang et al., 2019, 2025c). Spaceborne sensors, including MODIS, CALIPSO,  
99 TROPOMI, and OMI, provide global fields of aerosol optical depth (AOD) and  
100 vertical column densities (VCDs) for selected trace gases. However, their limited  
101 temporal sampling and spatial resolution preclude resolving the fine-scale diurnal  
102 variability and fine vertical structure of O<sub>3</sub> and HONO (Itahashi et al., 2020; Johnson  
103 et al., 2024; Torres et al., 2020a; Wang et al., 2025a). Chemical transport models  
104 (CTMs) and regional climate models (RCMs) can reproduce the spatiotemporal  
105 evolution of pollutants, but their performance depends critically on initial and  
106 boundary conditions, and uncertainties in vertical parameterizations—such as

107 turbulent mixing and chemical mechanisms—often lead to substantial biases in  
108 simulated profiles (Chambers et al., 2019; Kim et al., 2024; Li et al., 2021; Sekiya et  
109 al., 2025; Thürkow et al., 2024). Current in situ and remote-sensing techniques also  
110 have intrinsic limitations. Lidar systems provide high-resolution aerosol profiles but  
111 are restricted in detectable gaseous species and spatial coverage (Anon, 2023; Johnson  
112 et al., 2024; Torres et al., 2020b). Aircraft and balloon soundings yield detailed upper-  
113 air observations but are expensive and unsuitable for sustained, long-term monitoring  
114 (Johnson et al., 2024; Sekiya et al., 2025; Wang et al., 2025a; Yu et al., 2025). Tower  
115 measurements, while valuable near the surface, are height-limited and cannot capture  
116 the full vertical variability across the boundary layer (Chambers et al., 2019; Kim et  
117 al., 2024; Thürkow et al., 2024).

118 To address the observational limitations and scientific questions outlined above,  
119 we developed a comprehensive dataset of vertical profiles of HONO, O<sub>3</sub>, and their  
120 photolysis frequencies using the Chinese Hyperspectral Vertical Remote Sensing  
121 Network. The primary objective is to resolve the vertical structure of HONO and O<sub>3</sub>  
122 and to quantify the altitude-resolved production of OH radicals from their photolysis.  
123 This dataset fills a critical gap in vertical observations of key photochemical species  
124 over China and provides a unique basis for assessing the contribution of HONO  
125 photolysis to boundary-layer OH budget, the vertical characteristics of O<sub>3</sub> formation,  
126 and the role of aerosols in modulating photolysis rates. The dataset comprises  
127 measurements from 22 ground-based sites across five major regions of China—North,  
128 East, Southwest, South, and Central China—collected during 2021–2024. Its core  
129 products are high-temporal-resolution vertical profiles of HONO and O<sub>3</sub> spanning 0–4  
130 km. Public release of this dataset will enable systematic investigations of the  
131 unresolved sources of HONO in the boundary layer and the vertical variability in O<sub>3</sub>  
132 production sensitivity. When combined with numerical models, the high-resolution  
133 vertical information can be used to evaluate and refine photochemical mechanisms,  
134 quantify the contribution of HONO photolysis to the tropospheric OH budget, and  
135 reduce uncertainties in vertical parameterizations. These advances will, in turn,  
136 support robust source attribution of O<sub>3</sub> pollution and inform the development of  
137 coordinated regional control strategies for PM<sub>2.5</sub> and O<sub>3</sub>. The following sections  
138 describe the site distribution, observational and retrieval methods, and the seasonal  
139 and diurnal features of the HONO and O<sub>3</sub> vertical structures revealed by this dataset.

140

## 141 **2. Method**

### 142 **2.1 Description of the monitoring site**

143 The dataset is derived from 22 hyperspectral ground-based vertical remote  
144 sensing stations distributed across five major regions of China—North, East,  
145 Southwest, South, and Central China—forming an integrated network that samples a  
146 wide range of representative atmospheric environments (Table 1). The sites span  
147 urban cores, urban–suburban transition zones, regional background areas, coastal and  
148 land–sea interaction regions, as well as plateau, mountain, and basin settings, thereby

149 providing a three-dimensional observational framework for key photochemical  
150 species. In North China, stations at the Chinese Academy of Meteorological Sciences  
151 (CAMS1, CAMS2) and the University of Chinese Academy of Sciences (UCAS),  
152 located within Beijing (~100–120 m a.s.l.), characterize the heavily urbanized and  
153 industrialized core of the Beijing–Tianjin–Hebei megacity cluster. The Wangdu (WD)  
154 site in suburban Baoding represents regional background conditions, whereas the  
155 Shijiazhuang Luancheng (SJZ\_LC) site was included to better resolve pollution  
156 features specific to industrial cities. The Shanxi University (SXU) site in the Taihang  
157 Mountains (780 m a.s.l.) provides critical constraints on pollutant formation and  
158 transport between mountainous terrain and adjacent plains. In East China, stations are  
159 distributed across the Yangtze River Delta and its hinterland, covering topography  
160 from coastal lowlands to inland mountains. The summit of Mount Tai (TS; 1,500 m  
161 a.s.l.) offers vertical profiles under relatively clean, high-altitude background  
162 conditions. The Nanjing University of Information Science and Technology (NUIST)  
163 site represents a densely populated and economically developed urban environment,  
164 while sites at Huaibei Normal University (HNU), Anhui University (AHU), and  
165 Changfeng (CF) in Anhui Province (30–35 m a.s.l.) capture urban–suburban transition  
166 regimes. Southwest China is represented by the Chengdu Academy of Environmental  
167 Sciences (CDAES; 505 m a.s.l.) on the Chengdu Plain and the Chongqing (CQ; 332  
168 m a.s.l.) site within the Sichuan Basin. These stations are strategically located to  
169 investigate pollutant accumulation and transport under high-humidity conditions and  
170 strong topographic confinement, and to probe photochemical processes in complex  
171 terrain. In South China, a dense network was established over the Pearl River Delta  
172 megacity region. In addition to sites at the Guangzhou Institute of Geochemistry (GIG)  
173 and the Southern University of Science and Technology (SUST) in Shenzhen,  
174 multiple stations in Guangzhou (Zhuliao, Nansha, Timian, Gongyuan, and  
175 Daxuecheng; 15–155 m a.s.l.) form an intra-urban array. This configuration allows  
176 detailed examination of the combined influences of land–sea breezes, anthropogenic  
177 emissions, and local meteorology on the vertical distributions of HONO and O<sub>3</sub>.  
178 Central China is represented by the Luoyang (LY) site, located in the middle reaches  
179 of the Yellow River within a mixed industrial–agricultural region, providing key  
180 constraints on regional transport and accumulation over the central plains. Together,  
181 the broad geographic coverage and pronounced contrasts in elevation and surface type  
182 make this network well suited to resolve the vertical distributions of aerosols, HONO,  
183 and O<sub>3</sub> across urban, suburban, coastal, mountainous, and basin environments. It thus  
184 offers a robust observational basis for investigating the dynamics of photochemical air  
185 pollution over major regions of China.

186 Table 1. Geographic information of the stations in the Chinese Hyperspectral Ground-  
187 Based Vertical Remote Sensing Network.

Region	Site (code)	Longitude (° E)	Latitude (° N)	Altitude (m)
North China	Chinese Academy of Meteorological Sciences (CAMS1)	116.32	39.94	100
	Chinese Academy of Meteorological	116.32	39.94	100

	Sciences (CAMSS2)			
	University of Chinese Academy of Sciences (UCAS)	116.67	40.4	120
	Wangdu (WD)	115.15	38.17	35
	Shijiazhuang_Luancheng (SJZ_LC)	114.61	37.91	70
	Shanxi University (SXU)	112.58	37.63	780
	Taishan (TS)	117.1	36.25	1500
	Nanjing University of Information Science and Technology (NUIST)	118.71	32.2	73
East China	Lin'an (LA)	119.75	30.3	140
	HuaiBei Normal University (HNU)	116.8	33.98	35
	Anhui University (AHU)	117.18	31.77	30
	Changfeng (CF)	117.18	32.21	30
Southwest China	Chengdu Academy of Environmental Sciences (CDAES)	104.04	30.65	505
	Chongqing (CQ)	106.5	29.6	332
	Guangzhou Institute of Geochemistry (GIG)	113.35	23.15	30
	Southern University of Science and Technology (SUST)	113.99	22.59	40
South China	Guangzhou_Zhuliao (GZ_ZL)	113.34	23.36	20
	Guangzhou_Nansha (GZ_NS)	113.61	22.77	15
	Guangzhou_Timian (GZ_TM)	113.29	23.55	155
	Guangzhou_Gongyuan (GZ_GY)	113.26	23.13	15
	Guangzhou_Daxuecheng (GZ_DXC)	113.39	23.04	10
Central China	Luoyang (LY)	112.45	34.67	100

188

189

## 2.2 Instrument setup

190

191

192

193

194

195

196

197

198

199

200

201

202

203

204

205

206

207

208

## 2.3 Spectral retrieval

209

210

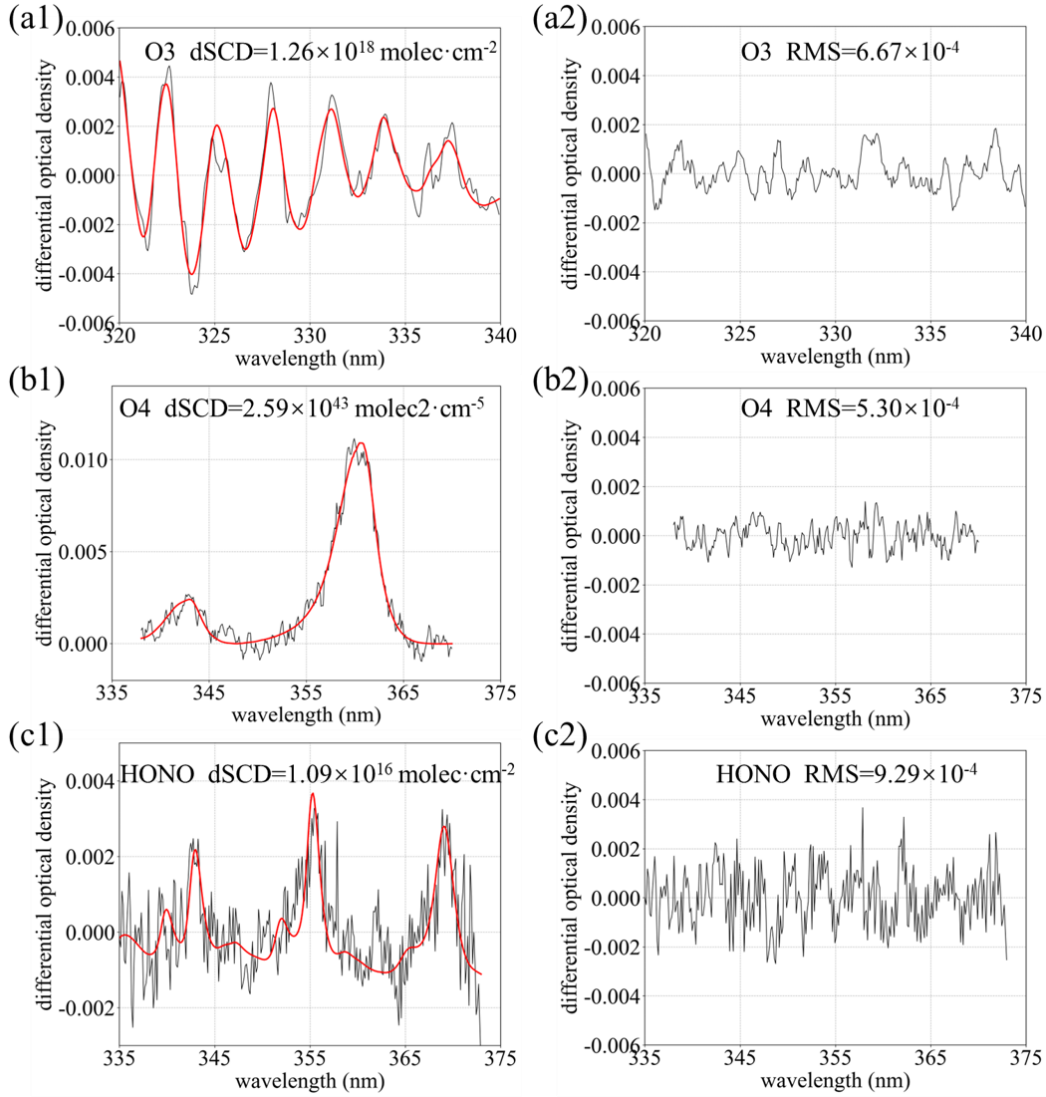
Ultraviolet–visible spectra measured by the ground-based instruments were analysed with the QDOAS software (version 3.2) developed by BIRA-IASB.

211 Differential optical absorption spectroscopy (DOAS) was applied to retrieve the  
 212 differential slant column densities (DSCDs) of the oxygen dimer ( $O_4$ ),  $O_3$ , and HONO.  
 213 For each elevation scan, the zenith spectrum ( $90^\circ$  elevation) acquired within the same  
 214 scanning sequence was used as the reference and subtracted from spectra at lower  
 215 elevation angles, thereby isolating the narrow-band absorption features of trace gases  
 216 from broadband structures and enabling robust retrieval of target species. The fitting  
 217 settings follow Xing et al. (2021, 2024a, b) and are summarized in Table 2. To  
 218 account for the Ring effect arising from rotational Raman scattering and Fraunhofer  
 219 line filling-in, a Ring spectrum calculated with DOASIS was included in the fit.  
 220 Broadband spectral structures were represented and removed using a fifth-order  
 221 polynomial. This allowing accurate separation of narrow-band molecular absorption.  
 222 Strict quality control was applied: only retrievals with a root-mean-square (RMS)  
 223 fitting residual below  $1 \times 10^{-3}$  were retained, ensuring the robustness and stability of  
 224 the dataset. Representative spectral fits and residuals for  $O_4$ ,  $O_3$ , and HONO are  
 225 shown in Figure 1.

226 Table 2. Detailed retrieval settings for  $O_4$ ,  $O_3$ , and HONO.

Parameter	Data source	Fitting interval		
		$O_4$	$O_3$	HONO
Wavelength range		338–370 nm	320–340 nm	335–373 nm
$NO_2$	220 K, $I_0^*$ correction (SCD of $10^{17}$ molec·cm $^{-2}$ ); (Vandaele et al., 1998)	√	×	√
$NO_2$	298 K, $I_0$ correction (SCD of $10^{17}$ molec·cm $^{-2}$ ); (Vandaele et al., 1998)	√	√	√
$O_3$	223 K, $I_0$ correction (SCD of $10^{18}$ molec·cm $^{-2}$ ); (Serdyuchenko et al., 2014)	√	√	√
$O_3$	243 K, $I_0$ correction (SCD of $10^{18}$ molec·cm $^{-2}$ ); (Serdyuchenko et al., 2014)	×	×	√
$O_3$	293 K, $I_0$ correction (SCD of $10^{18}$ molec·cm $^{-2}$ ); (Serdyuchenko et al., 2014)	√	√	×
$O_4$	293 K, $I_0$ correction (SCD of $3 \times 10^{43}$ molec $^2$ ·cm $^{-5}$ ); (Thalman and Volkamer, 2013)	√	√	√
HCHO	293 K, $I_0$ correction (SCD of $5 \times 10^{15}$ molec·cm $^{-2}$ ); (Orphal and Chance, 2003)	√	√	√
BrO	273 K, $I_0$ correction (SCD of $10^{13}$ molec·cm $^{-2}$ ); (Fleischmann et al., 2004)	√	×	√
Ring	Ring spectra calculated with DOASIS	√	√	√
HONO	$I_0$ correction (SCD of $10^{15}$ molec·cm $^{-2}$ );(Stutz et al., 2000)	×	×	√
Polynomial degree		5	5	5
Intensity offset		Constant	Constant	No

227 \* Solar  $I_0$  correction, Aliwell et al.(2002).



228

229 Figure 1. (a1) O<sub>3</sub>, (b1) O<sub>4</sub>, and (c1) HONO DOAS fitting examples; (a2) O<sub>3</sub>, (b2) O<sub>4</sub>,  
 230 and (c2) HONO fitting residuals.

231

## 232 2.4 Vertical profile retrieval algorithm

233 Vertical profiles of aerosols and trace gases (HONO and O<sub>3</sub>) were retrieved using  
 234 an inversion framework based on the optimal estimation method (OEM). The forward  
 235 radiative transfer calculations were performed with the linearized pseudo-spherical  
 236 vector discrete ordinate model VLIDORT (Spurr, 2006). The posterior state vector  $\mathbf{x}$   
 237 was obtained by minimizing the cost function  $\chi^2$ :

$$238 \quad \chi^2 = (\mathbf{y} - \mathbf{F}(\mathbf{x}, \mathbf{b}))^T \mathbf{S}_\varepsilon^{-1} (\mathbf{y} - \mathbf{F}(\mathbf{x}, \mathbf{b})) + (\mathbf{x} - \mathbf{x}_a)^T \mathbf{S}_a^{-1} (\mathbf{x} - \mathbf{x}_a) \quad (1)$$

239 where  $\mathbf{y}$  denotes the measured DSCDs,  $\mathbf{F}(\mathbf{x}, \mathbf{b})$  is the forward model,  $\mathbf{b}$  represents  
 240 ancillary meteorological parameters (e.g., temperature, pressure, single-scattering  
 241 albedo, and asymmetry factor),  $\mathbf{x}_a$  is the a priori state vector,  $\mathbf{S}_\varepsilon$  is the measurement  
 242 error covariance matrix, and  $\mathbf{S}_a$  is the a priori covariance matrix. For both aerosols  
 243 and trace gases, the a priori vertical profiles were assumed to decrease exponentially

244 with altitude, reflecting the characteristic rapid decay of pollutant concentrations  
245 within the planetary boundary layer. Because the absorption of the O<sub>4</sub> is strongly  
246 linked to aerosol optical properties, aerosol vertical profiles were first retrieved from  
247 multi-elevation O<sub>4</sub> DSCDs and subsequently used as inputs to the forward model for  
248 the retrieval of O<sub>3</sub> and HONO profiles. The atmosphere from the surface to 4 km was  
249 discretized into 20 layers with a vertical resolution of 200 m (Xing et al., 2024b).  
250 Retrievals were subjected to strict quality control: profiles with degrees of freedom  
251 (DOF) below 1.0,  $\chi^2$  values exceeding 200, or relative uncertainties greater than 50%  
252 were excluded from further analysis.

253

## 254 **2.5 TUV model**

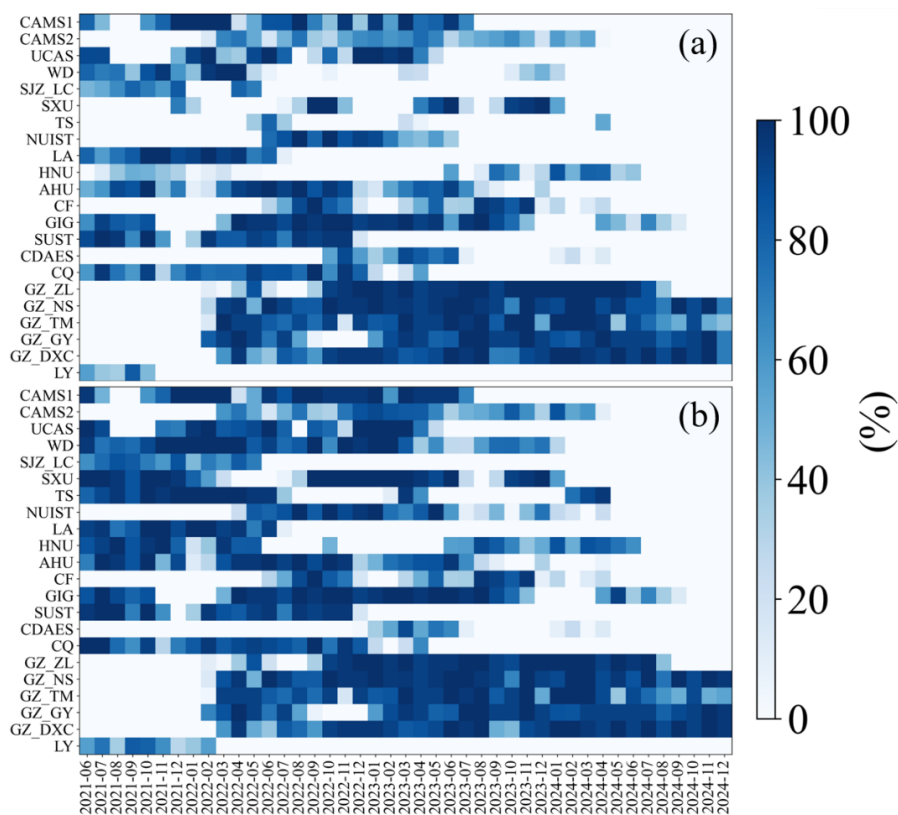
255 Photolysis rates of HONO and O<sub>3</sub> were computed with the Tropospheric  
256 Ultraviolet and Visible (TUV) radiative transfer model developed by NCAR, which is  
257 based on rigorous radiative transfer theory and implemented in FORTRAN  
258 (<https://www2.acom.ucar.edu/modeling/tropospheric>, last access: 26 January 2026).  
259 The TUV model simulates the propagation of solar radiation in the troposphere under  
260 prescribed optical and chemical conditions and provides spectrally resolved  
261 photolysis frequencies for key atmospheric reactions. These rates were used to  
262 quantify the contributions of HONO and O<sub>3</sub> photolysis to OH production. Model  
263 inputs included AOD at ~361 nm derived from MAX-DOAS-retrieved aerosol  
264 extinction profiles, total ozone column from daily TROPOMI observations (typically  
265 260–280 DU), and single-scattering albedo (SSA) constrained by regression analyses  
266 of O<sub>4</sub> absorptions at 361 and 477 nm (Xing et al., 2019).

267

## 268 **3. Vertical profile observations of atmospheric composition**

269 Figure 2 summarizes the monthly completeness of O<sub>3</sub> and HONO vertical profile  
270 measurements at 22 sites from 2021 to 2024. Shading denotes the fraction of valid  
271 observations, with 100% indicating uninterrupted daytime measurements and  
272 successful profile retrievals throughout the month. Because stations were  
273 commissioned at different times and operated under varying maintenance and field  
274 conditions, the available observation periods differ among sites. Most stations provide  
275 long, continuous time series of both HONO and O<sub>3</sub>. More than 85% of the sites had  
276 operational histories spanning over one year, and 60% for more than two years,  
277 although these periods may include intermittent data gaps due to maintenance,  
278 weather, or technical issues, with only quality-controlled valid profiles retained in the  
279 dataset, demonstrating the temporal stability of the network. This coverage enables  
280 robust characterization of seasonal and diurnal variability under diverse climatic  
281 regimes and emission backgrounds. Although a few sites had shorter operational  
282 periods owing to instrument commissioning and field constraints, they still delivered  
283 several months of continuous high-quality data, which are valuable for regional  
284 intercomparison and support analyses of long-term trends and photochemical  
285 processes. Isolated months with missing or incomplete data occur at some sites,

286 primarily because of unavoidable factors such as instrument maintenance, power  
 287 interruptions, persistent cloud or precipitation, and quality-control filtering (e.g.,  
 288 excessive fitting residuals or low DOF in the retrievals).

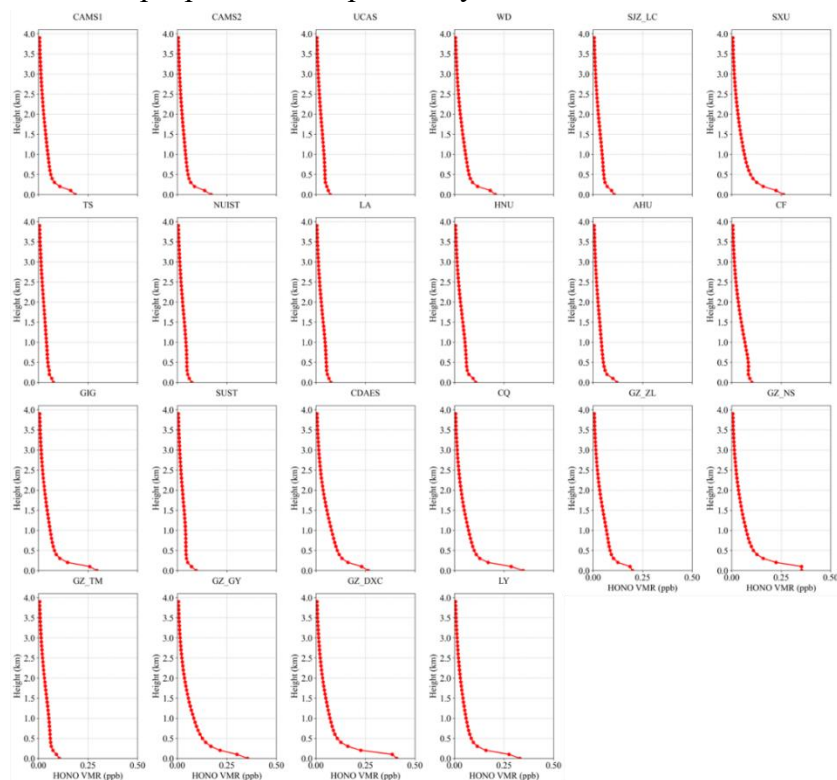


289  
 290 Figure 2. Monthly data completeness of the vertical profiles of (a) O<sub>3</sub> and (b) HONO.  
 291

### 292 3.1 HONO

293 Figure 3 presents the 2021–2024 mean vertical profiles of HONO across all sites.  
 294 At every location, HONO is strongly enriched near the surface and decreases rapidly  
 295 with height, following an approximately exponential decay. This structure is  
 296 characteristic of a boundary-layer-dominated species controlled by ground-based  
 297 sources (Li et al., 2025b; Meng et al., 2020; Xing et al., 2024c; Xu et al., 2021). Peak  
 298 mixing ratios occur within the lowest 0–0.5 km, decline sharply between 0.5 and 1.5  
 299 km, and generally fall to regional background or near the detection limit above 2 km  
 300 (<0.05–0.1 ppb), becoming negligible by 4 km. Such steep gradients reflect dominant  
 301 near-surface emissions and nocturnal heterogeneous formation of HONO from NO<sub>2</sub>  
 302 on ground and aerosol surfaces, combined with its short photochemical lifetime and  
 303 rapid daytime photolysis, which preclude sustained accumulation in the free  
 304 troposphere (Li et al., 2025b; Meng et al., 2020; Xing et al., 2024a). Pronounced  
 305 regional contrasts are evident. Urban sites in North and East China (e.g., CAMS1,  
 306 CAMS2, WD, SXU, AHU) exhibit the highest near-surface HONO (0.3–0.5 ppb  
 307 below 0.3 km), followed by a rapid decrease to <0.1 ppb above 1 km. The sharp  
 308 vertical gradients and absence of secondary maxima aloft indicate strong control by  
 309 surface sources and nocturnal heterogeneous production, with efficient removal by

310 turbulent mixing and photolysis within the planetary boundary layer (Xu et al., 2021).  
 311 In contrast, background or relatively clean sites (e.g., TS, LA) show much lower  
 312 concentrations, with near-surface values typically <0.2 ppb and a monotonic decrease  
 313 with altitude, consistent with weak local emissions and dominance of regional  
 314 background (Garcia-Nieto et al., 2018b; Li et al., 2025b). Sites in South and  
 315 Southwest China (e.g., GZ\_ZL, GZ\_NS, GZ\_DXC, CQ, CDAES) display a similar  
 316 monotonic decay: elevated HONO confined to the lowest 0–0.5 km and rapid  
 317 attenuation to background levels above 1–2 km, without a distinct mid-level  
 318 enhancement. Although near-surface mixing ratios at some locations (e.g., GZ\_DXC,  
 319 CQ) approach or slightly exceed 0.3 ppb, their vertical decay rates are comparable to  
 320 those at northern and eastern urban sites. This indicates that, even under high  
 321 humidity or complex topography, HONO remains largely restricted to the lower  
 322 boundary layer, governed by its short lifetime, fast photolysis, and dilution by  
 323 convective mixing, while large-scale vertical transport contributes little to its  
 324 maintenance aloft (Li et al., 2025b; Xing et al., 2021b; Xu et al., 2021). Seasonal  
 325 mean profiles are shown in Figures S1–S4. Taken together, the regionally averaged  
 326 profiles consistently demonstrate strong near-surface accumulation and rapid vertical  
 327 attenuation of HONO. This confirms that HONO is a short-lived, boundary-layer-  
 328 derived reactive nitrogen species, tightly coupled to surface emissions and  
 329 heterogeneous chemistry. It therefore plays a key role in initiating early-morning OH  
 330 production and regulating boundary-layer oxidizing capacity, whereas its direct  
 331 impact in the free troposphere is comparatively minor.

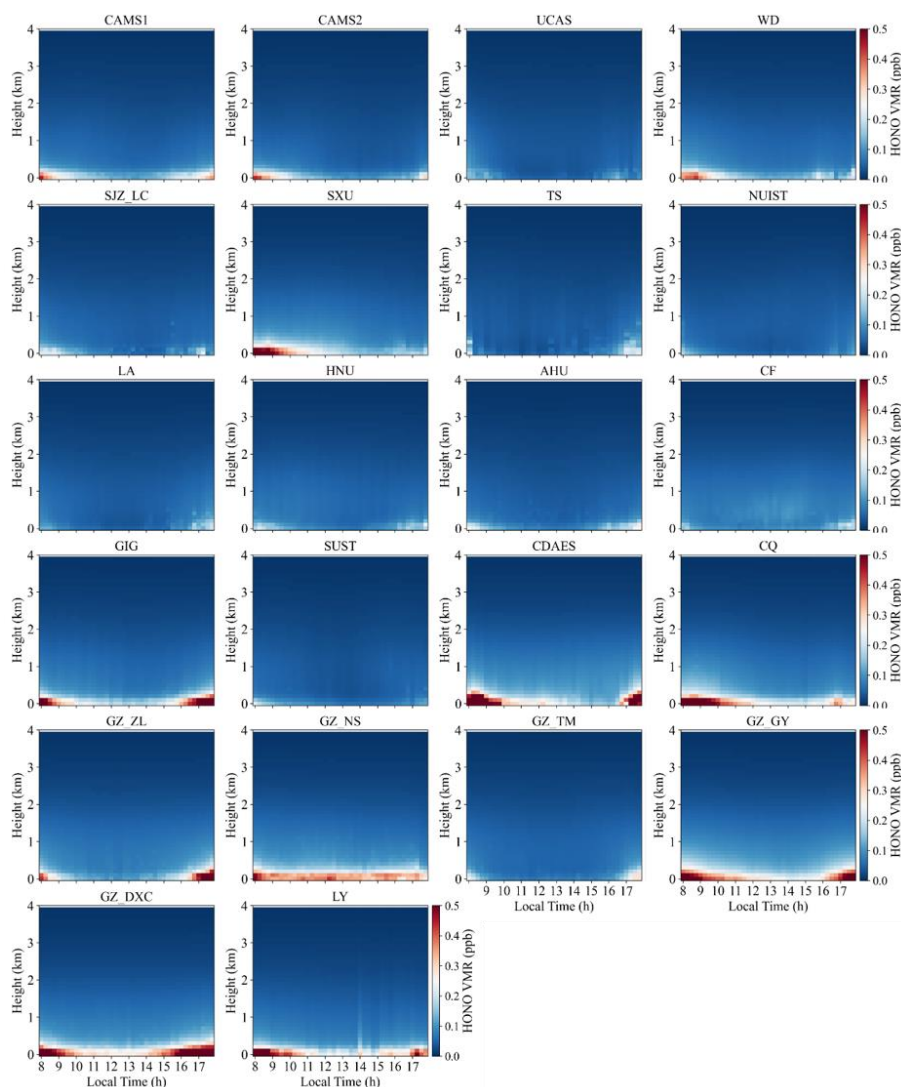


332 Figure 3. Mean vertical profiles of HONO averaged over 2021–2024.

333 Figure 4 illustrates the mean diurnal evolution of HONO. As a key reactive  
 334

335 nitrogen species, HONO exhibits vertical and temporal patterns that integrate the  
336 effects of surface emissions, heterogeneous and photochemical processes, and  
337 boundary-layer dynamics. Based on HONO data obtained from the hyperspectral  
338 vertical remote-sensing network, pronounced regional and site-specific patterns are  
339 observed. Across North China (CAMS1, CAMS2, UCAS, WD, SJZ\_LC and SXU),  
340 HONO exhibits a clear near-surface morning maximum followed by an afternoon  
341 minimum. At CAMS1 and CAMS2, the 0–1 km volume mixing ratio (VMR) peaks at  
342 08:00–10:00 local time (0.3–0.4 ppb) and decreases to 0.1–0.2 ppb by 14:00–16:00.  
343 This pattern reflects nocturnal accumulation driven by heterogeneous conversion of  
344 NO<sub>2</sub> on aerosol and ground surfaces (Liu et al., 2022a; Xing et al., 2023; Xuan et al.,  
345 2025b); after sunrise, enhanced solar radiation leads to the release and photochemical  
346 processing of HONO; meanwhile, morning rush-hour emissions of NO<sub>2</sub> and VOCs  
347 further promote HONO formation (Garcia-Nieto et al., 2018a; Zhang et al., 2025a). At  
348 the mountain site SXU, topography-induced temperature inversions enhance  
349 nighttime accumulation, yielding a more pronounced morning peak. In contrast,  
350 UCAS and WD, characterized by weaker anthropogenic emissions, show lower near-  
351 surface HONO levels and smaller diurnal amplitudes. In East China (TS, NUIST, LA,  
352 HNU, AHU and CF), urban sites display modest morning enhancements (0.2–0.3 ppb  
353 at 08:00–10:00) followed by afternoon decreases driven by boundary-layer growth  
354 and photolysis. At the high-altitude TS site (1500 m), HONO remains below 0.1 ppb  
355 with weak diurnal variability, reflecting clean background conditions and efficient  
356 vertical mixing. Sites with dense vegetation or agricultural land use (LA and CF) may  
357 receive contributions from biogenic VOC-related chemistry, but the overall pattern  
358 still features a subdued morning maximum (Liang et al., 2017; Ryan et al., 2018a; Xue  
359 et al., 2021; Ye et al., 2023a). At South China and Southwest China sites (GIG, SUST,  
360 CDAES, CQ and the Guangzhou cluster: GZ\_ZL, GZ\_NS, GZ\_TM, GZ\_GY and  
361 GZ\_DXC), warm and humid conditions together with basin or coastal circulations  
362 further modulate the diurnal cycle. Urban stations typically reach 0.3–0.5 ppb near the  
363 surface in the morning and decline to 0.1–0.2 ppb in the afternoon. In the Sichuan  
364 Basin (CQ), strong nocturnal inversions favour HONO accumulation, producing  
365 slightly higher morning peaks (0.4–0.5 ppb). At coastal sites, land–sea breeze  
366 circulation leads to a transient morning enhancement followed by dilution by cleaner  
367 marine air masses. At the Central China site LY, the diurnal pattern resembles that in  
368 North and South China, with a clear morning maximum and lower concentrations in  
369 the afternoon associated with boundary-layer development. Seasonal mean diurnal  
370 vertical profiles are shown in Figures S5–S8. Overall, the diurnal cycle of HONO is  
371 governed by three coupled processes: (i) nocturnal heterogeneous production from  
372 NO<sub>2</sub> on aerosol and surface substrates, which drives early-morning maxima (Li et al.,  
373 2025b; Meng et al., 2020; Xuan et al., 2024); (ii) enhancement by morning  
374 anthropogenic emissions of NO<sub>x</sub> and VOCs from traffic and industrial activities (Hao  
375 et al., 2020; Zhang et al., 2025a, 2023b); and (iii) rapid photolysis and boundary-layer  
376 dilution in the afternoon (Xing et al., 2021b, 2024a; Zhang et al., 2023b). Regional

377 contrasts arise from the combined effects of emission intensity, topography (basin,  
 378 mountain and coastal settings), and meteorological conditions, particularly  
 379 temperature inversions and ventilation efficiency (Li et al., 2025b; Xuan et al., 2024;  
 380 Zhang et al., 2025a).



381

382

Figure 4. Mean diurnal vertical profiles of HONO for 2021–2024.

383

### 384 3.2 O<sub>3</sub>

385

386

387

388

389

390

391

392

393

Figure 5 presents the mean vertical profiles of O<sub>3</sub> averaged over 2021–2024 for all sites. A consistent “low near the surface–high aloft” structure is observed, characterized by a monotonic increase or a weak S-shaped pattern. O<sub>3</sub> VMR are lowest in the lowest 0–0.5 km (20–60 ppb), rise rapidly between 1 and 2 km, and reach daytime maxima at 3–4 km (60–100 ppb). This vertical gradient agrees well with MAX-DOAS and ozone-sonde observations over eastern China and other regions worldwide (Couillard et al., 2021; Ji et al., 2023; Liao et al., 2024; Su et al., 2017; Wang et al., 2018; Zeng et al., 2023), and reflects the combined effects of strong near-surface NO<sub>2</sub> titration, dry deposition, and boundary-layer mixing that

394 suppress O<sub>3</sub>, together with photochemical production and regional transport that  
395 enhance O<sub>3</sub> aloft (Couillard et al., 2021; Donzelli and Suarez-Varela, 2024; Liao et al.,  
396 2024; Zeng et al., 2023; Zhu et al., 2025b). Within the boundary layer (0–1 km), O<sub>3</sub>  
397 generally increases sharply with height, and a weak local maximum or inflection is  
398 often found at 0.2–0.5 km. This contrasts with the vertical distributions of NO<sub>2</sub> and  
399 HCHO at the same sites, which show high near-surface concentrations dominated by  
400 emissions (Couillard et al., 2021; Hu et al., 2024; Hong et al., 2022; Jiao et al., 2025;  
401 Liu et al., 2023b). In contrast, O<sub>3</sub> is efficiently removed near the ground by nocturnal  
402 NO<sub>2</sub> titration and daytime surface deposition (Liao et al., 2024; Xing et al., 2022). At  
403 urban and suburban stations (e.g., UCAS and CF), O<sub>3</sub> in the lowest 0–0.3 km can  
404 decrease to 20–40 ppb, indicating strong titration by traffic and industry related NO<sub>2</sub>  
405 (Hu et al., 2024). Between 1 and 3 km, O<sub>3</sub> increases nearly monotonically at most  
406 sites, with the largest vertical gradient typically occurring around 2–3 km. This layer  
407 often corresponds to the daytime boundary-layer top or the nocturnal residual layer  
408 and represents a key altitude for regional photochemical accumulation and downward  
409 transport (He et al., 2023b; Liao et al., 2024; Zhu et al., 2025a). Numerous studies  
410 have shown that O<sub>3</sub>-rich air in the upper boundary layer and residual layer can be  
411 mixed downward during boundary-layer growth, and that O<sub>3</sub> stored aloft at night is re-  
412 entrained to the surface the following morning, making an important contribution to  
413 surface O<sub>3</sub> levels (Ancellet et al., 2024; Donzelli and Suarez-Varela, 2024; Liu et al.,  
414 2022b; Shi et al., 2022; Song et al., 2024; Wang et al., 2024b). At 3–4 km, O<sub>3</sub> VMR  
415 further increase and tend to level off, with some sites exhibiting distinct maxima. At  
416 these altitudes, the influence of surface NO<sub>2</sub> titration becomes negligible, whereas  
417 long-range transport and possible stratosphere–troposphere exchange start to play a  
418 role. Previous studies have shown that enhanced O<sub>3</sub> at 3–5 km over East Asia in  
419 spring and summer can partly arise from stratospheric intrusions and westerly long-  
420 range transport (Li et al., 2025a; Liao et al., 2024, 2025; Park et al., 2020). The  
421 pronounced O<sub>3</sub> enhancements observed at 3–4 km at sites such as CQ, GZ\_TM and  
422 SUST are therefore likely linked to free-tropospheric background O<sub>3</sub> and regional-  
423 scale transport processes. Seasonal mean O<sub>3</sub> vertical profiles are shown in Figures  
424 S9–S12.

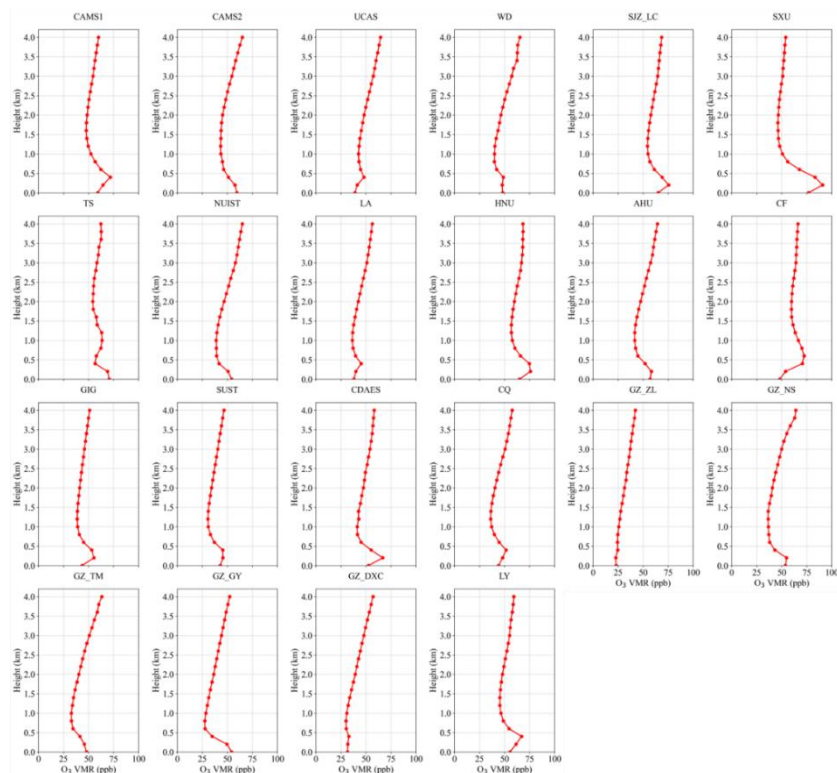


Figure 5. Mean vertical profiles of O<sub>3</sub> averaged over 2021–2024.

425

426

427

428

429

430

431

432

433

434

435

436

437

438

439

440

441

442

443

444

445

446

447

448

449

Figure 6 presents the mean diurnal evolution of O<sub>3</sub>. All sites exhibit pronounced daily cycles with clear regional contrasts. O<sub>3</sub> typically peaks in the morning (08:00–10:00) or in the early afternoon (12:00–15:00), in phase with the diurnal variation of solar irradiance and photochemical reaction rates (Xia et al., 2021; Yang et al., 2020). This behaviour is most evident in North and East China, whereas the cycle is weaker in South China, likely owing to persistently high temperature and humidity that modulate boundary-layer development and photochemistry (Zhou et al., 2022). At several sites (e.g., TS, CDAES and CQ), enhanced O<sub>3</sub> at 1–2 km during 12:00–15:00 points to the influence of local meteorology and emission distributions (Chen et al., 2023; Li et al., 2025a). In contrast, morning maxima at CAMS1, CAMS2, UCAS, NUIST and AHU reflect the rapid re-entrainment and photochemical processing of O<sub>3</sub> accumulated overnight after sunrise (David and Nair, 2011; Liao et al., 2023). The vertical structure of the diurnal cycle also differs markedly among regions. North China sites show strong near-surface variability, whereas peak O<sub>3</sub> in South China is generally lower, consistent with regional differences in pollution levels and meteorological conditions. Relatively high near-surface O<sub>3</sub> at GZ\_ZL and GZ\_NS is likely linked to local emissions combined with weak dispersion (Yang et al., 2020; Zhou et al., 2022). North China stations (CAMS1, CAMS2, UCAS, WD, SJZ\_LC and SXU) display a typical urban O<sub>3</sub> diurnal pattern. At CAMS1 and CAMS2, O<sub>3</sub> in the 0–1 km layer reaches 80–120 ppb in the morning (08:00–10:00) and decreases markedly in the early afternoon, reflecting rapid boundary-layer growth and photochemical loss after sunrise (David and Nair, 2011; Liao et al., 2023). UCAS and WD show similar morning maxima, whereas SJZ\_LC is characterized by lower and

450 more stable O<sub>3</sub>, indicative of relatively clean background conditions. At SXU, high  
451 morning O<sub>3</sub> (80–100 ppb) is followed by even higher afternoon levels (>100 ppb),  
452 pointing to strong in situ secondary production under intense photochemical activity  
453 (Wang et al., 2017; Xia et al., 2021). East China sites (TS, NUIST, LA, HNU, AHU  
454 and CF) exhibit more complex diurnal behaviour. At TS, O<sub>3</sub> peaks at 1–2 km during  
455 12:00–15:00 (80–100 ppb), suggesting an important role of vertical transport and  
456 local emissions. NUIST and AHU show morning maxima similar to those in North  
457 China, whereas LA maintains low and weakly varying O<sub>3</sub>, consistent with relatively  
458 clean conditions (Chen et al., 2024). At HNU, near-surface O<sub>3</sub> increases in the early  
459 afternoon (60–80 ppb), reflecting active photochemistry (Wang et al., 2025c). CF  
460 shows a pronounced afternoon peak (13:00–17:00, 80–120 ppb), indicating a strong  
461 influence of local sources (Xia et al., 2021; Yang et al., 2020). South China sites (GIG,  
462 SUST, GZ\_ZL, GZ\_NS, GZ\_TM, GZ\_GY and GZ\_DXC) differ substantially from  
463 those in the north and east. GIG exhibits low and weakly varying O<sub>3</sub>, representative of  
464 background conditions (Chen et al., 2024; Lin et al., 2022). The other sites show  
465 morning near-surface maxima (80–100 ppb at 08:00–10:00), followed by decreases  
466 associated with rapid boundary-layer development after sunrise (David and Nair, 2011;  
467 Liao et al., 2023), and enhanced O<sub>3</sub> at 3–4 km in the afternoon (13:00–17:00),  
468 highlighting the pronounced vertical structure of O<sub>3</sub> pollution in this region.  
469 Southwestern sites (CDAES and CQ) display distinct afternoon enhancements at 1–2  
470 km. At CDAES, O<sub>3</sub> reaches 80–120 ppb during 15:00–18:00, likely favored by high  
471 temperature and humidity that accelerate photochemical production (Yang et al., 2020;  
472 Zhang et al., 2022), while CQ shows a similar but weaker enhancement (60–80 ppb).  
473 The central China site LY exhibits morning near-surface maxima (60–80 ppb) and  
474 elevated O<sub>3</sub> at 2–4 km in the afternoon, characteristic of a typical urban diurnal cycle.  
475 Seasonal mean diurnal vertical profiles are shown in Figures S13–S16. These regional  
476 contrasts underline the differing controls on O<sub>3</sub> across China, with strong local  
477 photochemistry in North China, combined regional transport and sustained  
478 photochemical production in South China, and mixed influences of emissions and  
479 meteorology in East China.

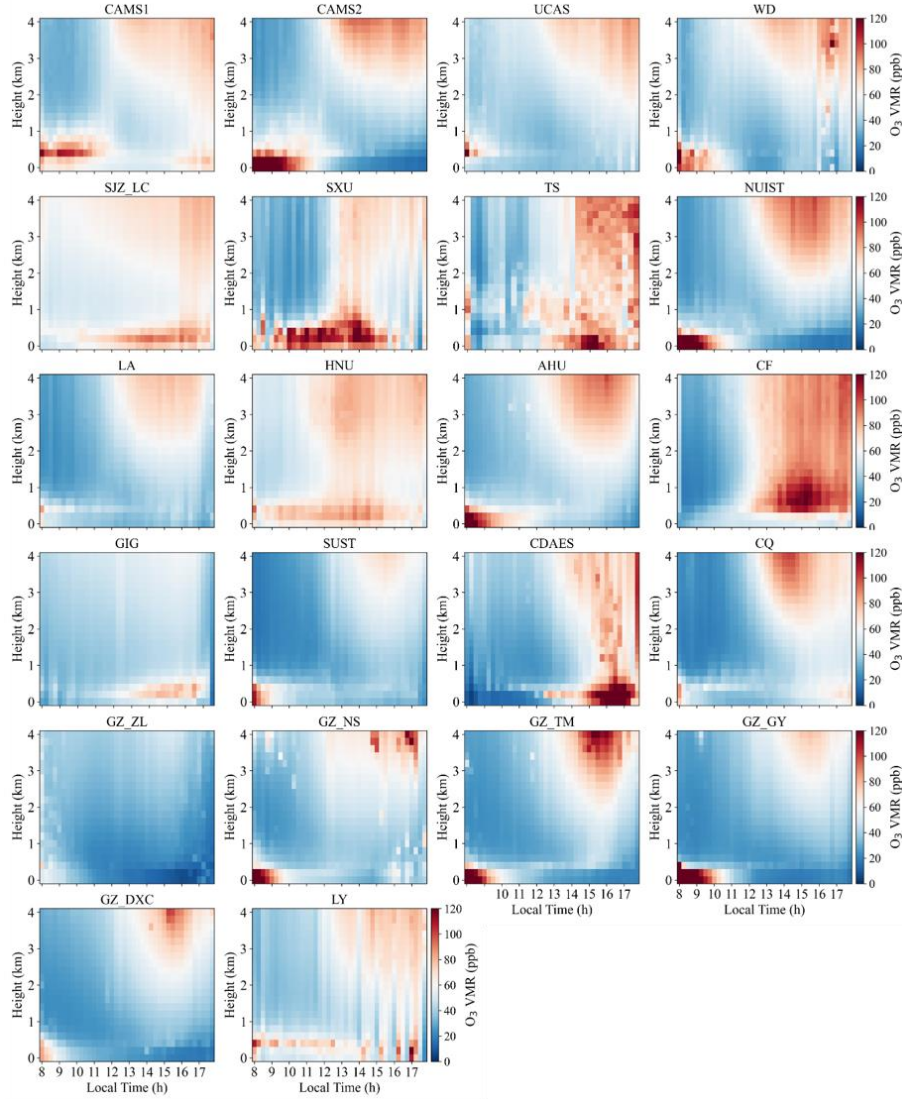


Figure 6. Mean diurnal vertical profiles of O<sub>3</sub> for 2021–2024.

### 3.3 OH production

Photolysis of HONO and O<sub>3</sub> constitutes a primary source of OH radicals and therefore controls the atmospheric oxidation capacity (AOC). To quantify the AOC at each site, we evaluated altitude-resolved OH production from HONO and O<sub>3</sub> using retrieved profiles combined with photolysis frequencies calculated by the TUV model. OH production from HONO and O<sub>3</sub> was computed from the following expressions.

$$P(OH)_{HONO} = J(HONO) \times [HONO] \quad (2)$$

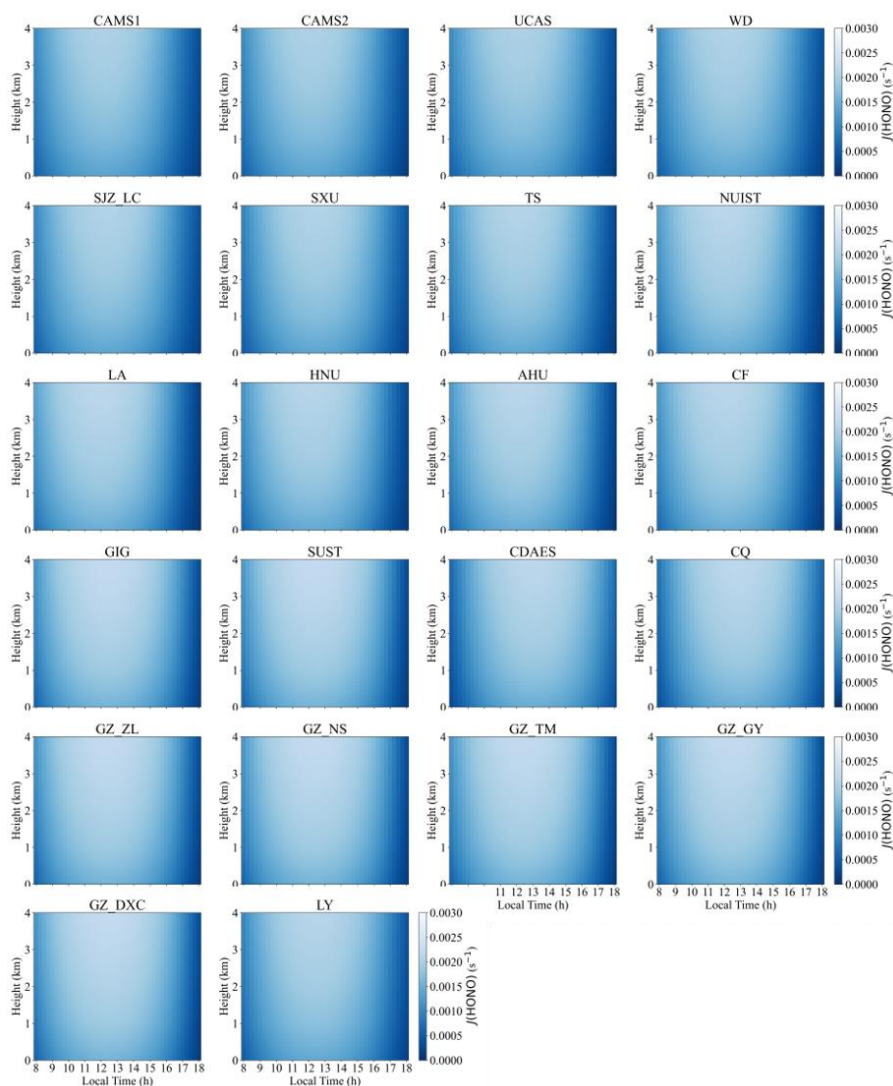
$$P(OH)_{O_3} = 2 \times f \times J(O(^1D)) \times [O_3] \quad (3)$$

Here,  $J(HONO)$  and  $J(O(^1D))$  are the photolysis rate coefficients of HONO and O<sub>3</sub>, respectively, obtained from the TUV model. O(<sup>1</sup>D) denotes electronically excited atomic oxygen produced by O<sub>3</sub> photodissociation, and  $f$  represents the branching fraction of the reaction  $O(^1D) + H_2O \rightarrow 2OH$ .  $[HONO]$  and  $[O_3]$  are the

495 concentrations of HONO and O<sub>3</sub> at each altitude level.

496 Figure 7 presents the mean diurnal vertical profiles of the HONO photolysis  
497 frequency, J(HONO), at 22 sites during 2021–2024; the corresponding seasonal mean  
498 diurnal variations are presented in Figures S17–S20. All sites exhibit a canonical  
499 photochemical pattern: J(HONO) increases rapidly after sunrise, reaches a maximum  
500 around local noon, and then gradually decreases with increasing solar zenith angle.  
501 Elevated values persist between 10:00 and 14:00 local time, with peak J(HONO)  
502 typically occurring near 12:00–13:00, indicating that HONO photolysis is primarily  
503 controlled by solar irradiance, in agreement with observations in Beijing and  
504 Guangzhou (He et al., 2023c; Ryan et al., 2018b). Vertically, J(HONO) increases  
505 systematically with altitude. Photolysis rates are relatively low in the near-surface  
506 layer (0–0.5 km), increase markedly in the upper mixed layer and lower free  
507 troposphere (approximately 1–3 km), and reach maxima between 2 and 4 km, with  
508 peak values around  $2.5 \times 10^{-3} \text{ s}^{-1}$ . This “weaker near the surface and stronger aloft”  
509 structure is highly consistent with the J(HONO) profiles reported by Xing et al.  
510 (2024a) and reflects the combined effects of aerosol attenuation of ultraviolet  
511 radiation in the lower atmosphere and enhanced shortwave actinic flux at higher  
512 altitudes (He et al., 2023c; Ryan et al., 2018b; Spataro and Ianniello, 2014). At the  
513 North China sites (CAMS1, CAMS2, UCAS, WD, SJZ\_LC, SXU), J(HONO) exhibits  
514 a pronounced diurnal cycle, increasing after sunrise with rising solar radiation,  
515 peaking at midday (12:00–14:00) at 0.0020–0.0025 s<sup>-1</sup>, and decreasing in the  
516 afternoon (14:00–18:00). The urban Beijing sites CAMS1 and CAMS2 show peak  
517 values of  $\sim 0.0025 \text{ s}^{-1}$ , comparable to those at other North China Plain stations (e.g.,  
518 UCAS and WD), reflecting strong photolysis under high HONO loading and  
519 favourable radiation conditions. At SJZ\_LC, located at the foothills of the Taihang  
520 Mountains, morning J(HONO) is slightly enhanced, likely owing to temperature  
521 inversions that modulate the vertical distribution of aerosols and actinic flux. The  
522 elevated site SXU (780 m a.s.l.) exhibits systematically higher J(HONO) than lowland  
523 stations, with a peak of  $\sim 0.0022 \text{ s}^{-1}$ , consistent with reduced aerosol extinction and  
524 stronger solar radiation at higher altitude. East China sites (TS, NUIST, LA, HNU,  
525 AHU, CF) display similar peak timing to North China but slightly lower magnitudes  
526 (0.0015–0.0025 s<sup>-1</sup>). For example, J(HONO) at NUIST peaks at  $\sim 0.0020 \text{ s}^{-1}$ , whereas  
527 the high-altitude background site TS (1500 m a.s.l.) reaches  $\sim 0.0021 \text{ s}^{-1}$ , consistent  
528 with enhanced actinic flux under cleaner atmospheric conditions. In South China  
529 (GIG, SUST, GZ\_ZL, GZ\_NS, GZ\_TM, GZ\_GY, GZ\_DXC), the maximum J(HONO)  
530 occurs slightly later in the day (13:00–15:00) and attains higher values (0.0020–  
531 0.0030 s<sup>-1</sup>). The highest peak is observed at GZ\_DXC ( $\sim 0.0030 \text{ s}^{-1}$ ), likely reflecting  
532 elevated HONO concentrations promoted by warm and humid conditions that favor  
533 heterogeneous formation. The southwestern basin site CQ shows a comparable peak  
534 ( $\sim 0.0025 \text{ s}^{-1}$ ), while the Central China site LY reaches  $\sim 0.0020 \text{ s}^{-1}$ , similar to values in  
535 North and East China. Overall, urban sites exhibit larger diurnal amplitudes and 20–  
536 40% higher J(HONO) maxima than mountain or clean-background sites, owing to

537 higher HONO abundances and aerosol loading that modulate the effective actinic flux.  
 538 This behaviour is fully consistent with previous findings from Beijing, Shanghai and  
 539 other megacities, which reported pronounced daytime enhancement of  $J(\text{HONO})$   
 540 under high- $\text{NO}_2$  and high-HONO conditions (He et al., 2023c; Spataro and Ianniello,  
 541 2014; Ye et al., 2023b).

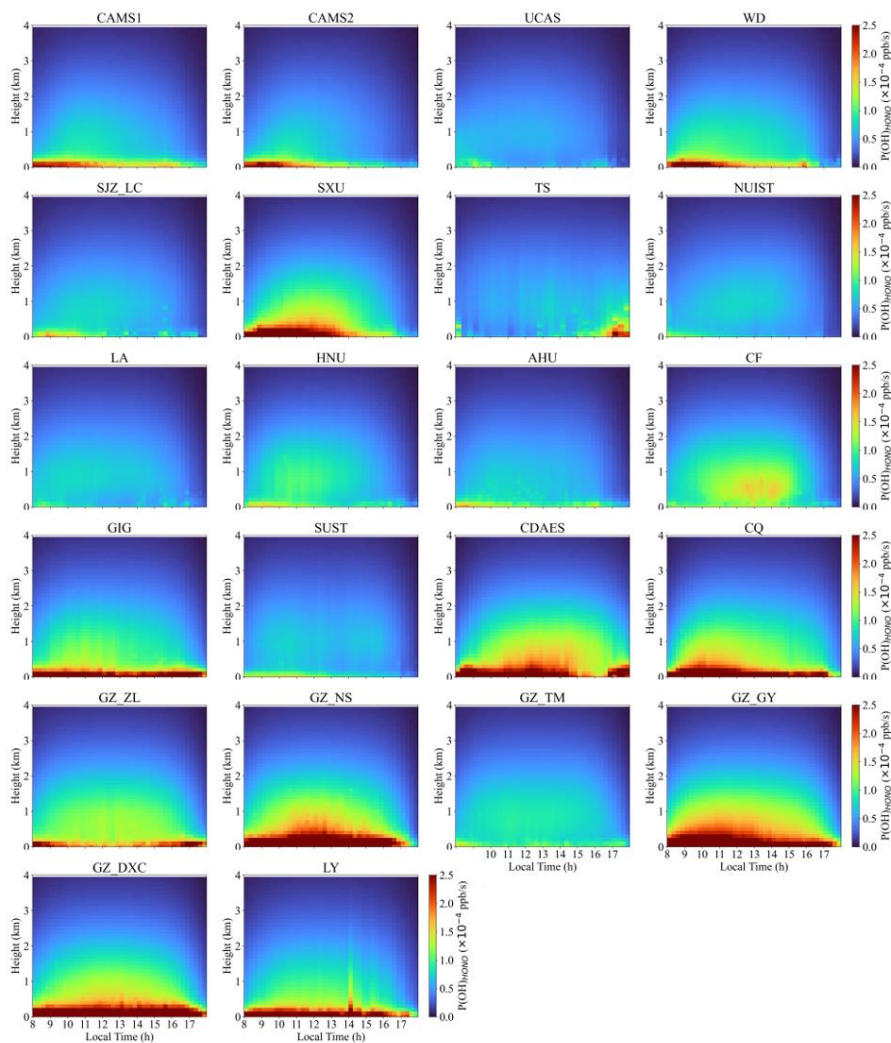


542

543 Figure 7. Mean diurnal vertical profiles of the HONO photolysis rate,  $J(\text{HONO})$ .

544 Figure 8 presents the mean diurnal vertical profiles of OH production from  
 545 HONO photolysis,  $P(\text{OH})_{\text{HONO}}$ , at 22 sites; the corresponding seasonal mean profiles  
 546 are shown in Figures S21–S24. At all sites,  $P(\text{OH})_{\text{HONO}}$  displays a pronounced  
 547 unimodal diurnal cycle, increasing rapidly after sunrise, peaking between 10:00 and  
 548 14:00, and declining thereafter. The peak timing closely follows the maximum of the  
 549  $J(\text{HONO})$ , whereas the peak altitude remains confined to the near-surface layer,  
 550 reflecting the strong surface enhancement of HONO. In the lower boundary layer (0–  
 551 0.5 km),  $P(\text{OH})_{\text{HONO}}$  attains its column maximum, with most sites peaking between  
 552 11:00 and 13:00 and reaching  $1.0 \times 10^{-4}$ – $5.5 \times 10^{-4}$   $\text{ppb} \cdot \text{s}^{-1}$ . For all stations,  $P(\text{OH})_{\text{HONO}}$   
 553 is largest within 0–1 km and decreases monotonically with height, consistent with the

554 preferential accumulation of HONO near the surface and the resulting localization of  
555 photochemically produced OH (He et al., 2023c; Li et al., 2025b; Xing et al., 2021b;  
556 Zhang et al., 2025a). Several sites, including SXU, CDAES, CQ, GZ\_NS, GZ\_GY,  
557 and GZ\_DXC, exhibit particularly strong OH production, with peak  $P(\text{OH})_{\text{HONO}}$   
558 commonly exceeding  $3.0 \times 10^{-4} \text{ ppb} \cdot \text{s}^{-1}$ . This reflects the combined effects of elevated  
559 HONO levels and intense solar radiation. At these locations, the high-  $P(\text{OH})_{\text{HONO}}$   
560 layer can extend to 1–2 km, indicating a deeper photochemically active region. This  
561 feature is consistent with earlier reports highlighting the substantial contribution of  
562 HONO to OH in the lower free troposphere (Aumont et al., 2003; R. Crilley et al.,  
563 2016; Xue et al., 2025; Zhang et al., 2025a). Vertically,  $P(\text{OH})_{\text{HONO}}$  decreases rapidly  
564 with altitude at all sites and is reduced to 20–40% of its surface value above 2 km,  
565 demonstrating that the impact of HONO photolysis on OH is largely confined to the  
566 boundary layer. In agreement with previous observations in Beijing and Guangzhou  
567 (Gu et al., 2022; Meng et al., 2020; Yu et al., 2022), HONO photolysis represents one  
568 of the dominant OH sources during the morning and around local noon, accounting  
569 for 30–60% of the daytime OH production near the surface (Song et al., 2023a; Tang  
570 et al., 2015). In the present study, several plateau sites show even larger relative  
571 contributions at midday, indicating that under conditions of low  $\text{NO}_2$  and strong solar  
572 irradiance, HONO photolysis becomes an especially efficient radical source,  
573 consistent with findings at Nam Co (Xing et al., 2024b). Regionally, North China sites  
574 (CAMS1, CAMS2, UCAS, WD, SJZ\_LC, and SXU) exhibit near-surface (0–1 km)  
575  $P(\text{OH})_{\text{HONO}}$  maxima between 12:00 and 14:00 local time, with values of  $1.0 \times 10^{-4}$ –  
576  $3.0 \times 10^{-4} \text{ ppb} \cdot \text{s}^{-1}$ . At CAMS1, the peak reaches  $\sim 1.5 \times 10^{-4} \text{ ppb} \cdot \text{s}^{-1}$ , whereas at SJZ\_LC,  
577 although nocturnal temperature inversions near the Taihang Mountains may favour  
578 HONO accumulation, the peak remains modest ( $\sim 1.2 \times 10^{-4} \text{ ppb} \cdot \text{s}^{-1}$ ) owing to weaker  
579 local emissions, comparable to UCAS and WD ( $1.0 \times 10^{-4}$ – $2.5 \times 10^{-4} \text{ ppb} \cdot \text{s}^{-1}$ ). At these  
580 sites,  $P(\text{OH})_{\text{HONO}}$  declines sharply with height and is substantially reduced above 1  
581 km, underscoring the near-surface confinement of both HONO and OH production  
582 from its photolysis. East China stations (TS, NUIST, LA, HNU, AHU, and CF) show  
583 similar peak times (12:00–14:00) but slightly lower magnitudes ( $1.0 \times 10^{-4}$ – $1.5 \times 10^{-4}$   
584  $\text{ppb} \cdot \text{s}^{-1}$ ). In South China (GIG, SUST, GZ\_ZL, GZ\_NS, GZ\_TM, GZ\_GY, and  
585 GZ\_DXC), peaks occur later (13:00–15:00) and are substantially higher ( $2.5 \times 10^{-4}$ –  
586  $5.5 \times 10^{-4} \text{ ppb} \cdot \text{s}^{-1}$ ), consistent with enhanced heterogeneous HONO formation under  
587 warm and humid conditions. Southwest China sites (CDAES and CQ) reach peak  
588 values of  $\sim 3.5 \times 10^{-4} \text{ ppb} \cdot \text{s}^{-1}$ , comparable to those in South China, likely owing to  
589 basin-induced HONO accumulation and vigorous photochemistry. In Central China  
590 (LY), the peak ( $\sim 2.7 \times 10^{-4} \text{ ppb} \cdot \text{s}^{-1}$ ) is similar to that in North and East China,  
591 indicating broadly comparable HONO sources and photolysis efficiencies across these  
592 regions.

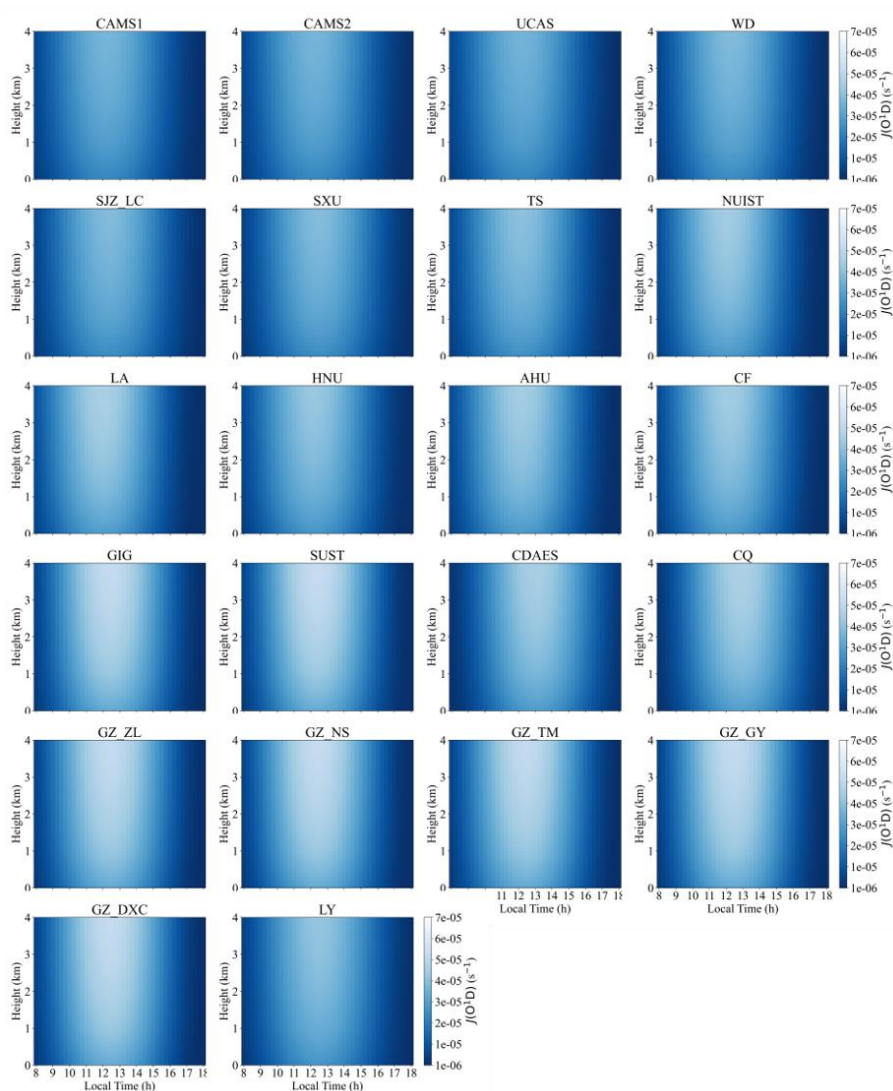


593

594 Figure 8. Mean vertical profiles of OH radicals generated by HONO photolysis.

595 Figure 9 presents the  $O_3$  photolysis frequency,  $J(O(^1D))$ , at all 22 sites follows a  
 596 pronounced diurnal cycle, with maxima consistently occurring between 12:00 and  
 597 14:00 local time. Seasonal mean diurnal variations are presented in Figures S25–S28.  
 598 In North China (CAMS1, CAMS2, UCAS, WD, SJZ\_LC, and SXU), near-surface  
 599 peak  $J(O(^1D))$  ranges from  $\sim 5 \times 10^{-5}$  to  $7 \times 10^{-5} \text{ s}^{-1}$ . The urban sites CAMS1, CAMS2,  
 600 UCAS, and WD reach the highest values ( $\sim 6 \times 10^{-5}$ – $7 \times 10^{-5} \text{ s}^{-1}$ ) at midday. At SJZ\_LC,  
 601 located at the foothills of the Taihang Mountains, nocturnal temperature inversions  
 602 can favor  $O_3$  accumulation (Guo et al., 2024b; He et al., 2021), but the peak remains  
 603 slightly lower ( $\sim 5 \times 10^{-5}$ – $6 \times 10^{-5} \text{ s}^{-1}$ ), likely constrained by local emissions. At the  
 604 higher-altitude SXU site (780 m a.s.l.), near-surface  $J(O(^1D))$  is reduced ( $\sim 4 \times 10^{-5}$ –  
 605  $5 \times 10^{-5} \text{ s}^{-1}$ ). Overall, urban stations exhibit larger  $J(O(^1D))$  than suburban and rural  
 606 sites, reflecting higher  $O_3$  levels driven by anthropogenic precursors and consistent  
 607 with reported regional contrasts (Fardilah et al., 2023; Guo et al., 2024a; Qiu et al.,  
 608 2025). In East China (TS, NUIST, LA, HNU, AHU, and CF), near-surface  $J(O(^1D))$   
 609 peaks at  $\sim 4 \times 10^{-5}$ – $6 \times 10^{-5} \text{ s}^{-1}$ , with urban sites such as NUIST and AHU reaching  
 610  $\sim 5 \times 10^{-5}$ – $6 \times 10^{-5} \text{ s}^{-1}$  at noon. In contrast, the high-altitude TS site (1500 m a.s.l.)

611 shows lower values ( $\sim 3 \times 10^{-5}$ – $4 \times 10^{-5} \text{ s}^{-1}$ ), consistent with its lower O<sub>3</sub> burden and  
 612 cleaner background conditions. South China stations (GIG, SUST, GZ\_ZL, GZ\_NS,  
 613 GZ\_TM, GZ\_GY, and GZ\_DXC) display slightly higher peak J(O(<sup>1</sup>D))) ( $\sim 6 \times 10^{-5}$ –  
 614  $7 \times 10^{-5} \text{ s}^{-1}$ ), in line with enhanced O<sub>3</sub> production under warm and humid subtropical  
 615 conditions (Lu et al., 2025; Song et al., 2026; Zhang et al., 2025b). In Southwest  
 616 China (CDAES and CQ), peak values ( $\sim 5 \times 10^{-5}$ – $6 \times 10^{-5} \text{ s}^{-1}$ ) are comparable to those in  
 617 South China, likely driven by basin topography that favors O<sub>3</sub> accumulation and  
 618 vigorous photochemistry (Qiao et al., 2019; Shu et al., 2023; Wang et al., 2024a). The  
 619 Central China site LY exhibits slightly lower peaks ( $\sim 4 \times 10^{-5}$ – $5 \times 10^{-5} \text{ s}^{-1}$ ), similar to  
 620 North and East China, indicating broadly comparable O<sub>3</sub> sources and photolysis  
 621 efficiencies across these regions.



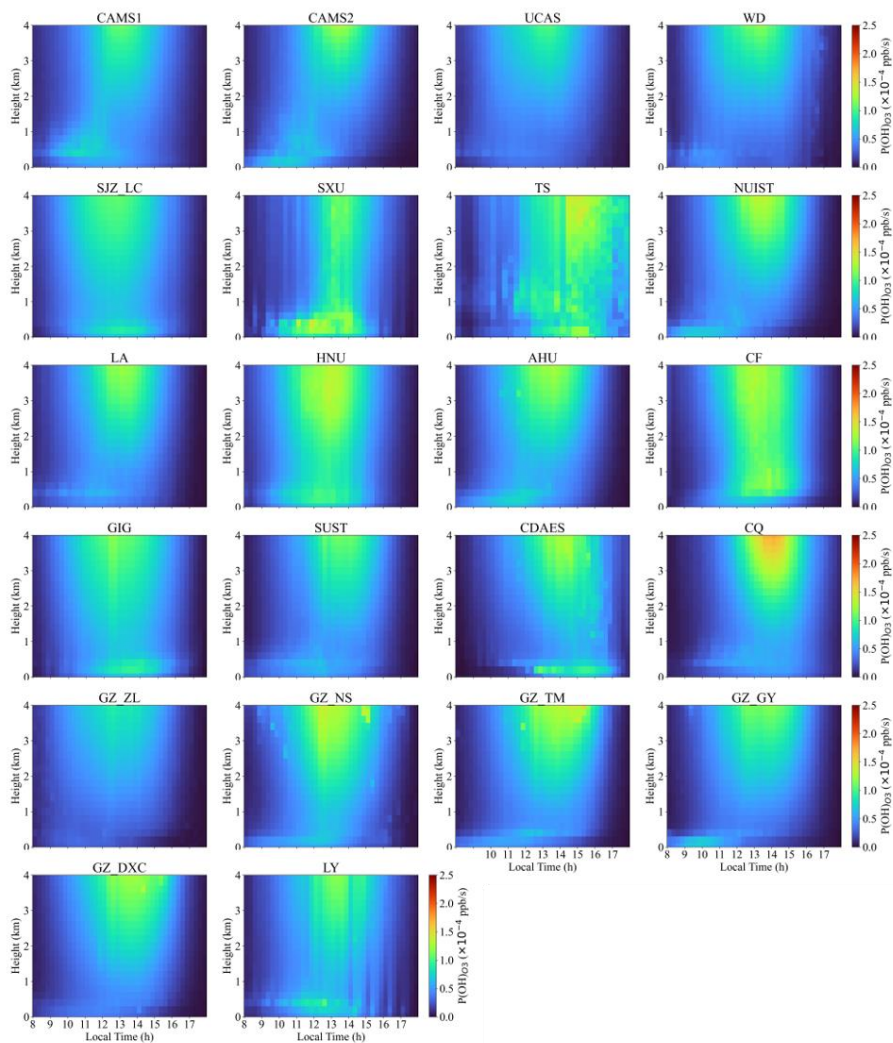
622

623 Figure 9. Mean diurnal vertical profiles of the O<sub>3</sub> photolysis rate, J(O(<sup>1</sup>D))).

624

625 Figure 10 presents the mean diurnal vertical profiles of the OH production rate  
 626 from ozone photolysis, P(OH)<sub>O<sub>3</sub></sub>, at the 22 sites, and seasonal mean diurnal variations  
 627 are presented in Figures S29–S32. All sites exhibit a pronounced unimodal diurnal  
 cycle, with P(OH)<sub>O<sub>3</sub></sub> increasing rapidly after sunrise, peaking between 12:00 and

628 14:00 local time, and declining thereafter. The vertical location of the maxima varies  
629 markedly among sites: at some, enhanced production is confined to the near-surface  
630 layer (0–0.5 km), whereas at others distinct maxima occur at 3–4 km, indicating  
631 substantial regional differences in photochemical regimes. Peak  $P(OH)O_3$  spans  
632  $0.5 \times 10^{-4}$ – $2.0 \times 10^{-4}$   $ppb \cdot s^{-1}$  across the network. In North China (CAMS1, CAMS2,  
633 UCAS, WD, SJZ\_LC, and SXU), near-surface  $P(OH)O_3$  during 12:00–14:00 reaches  
634  $1.0 \times 10^{-4}$ – $2.0 \times 10^{-4}$   $ppb \cdot s^{-1}$ . The urban sites CAMS1, CAMS2, UCAS, and WD show  
635 the highest values ( $1.5 \times 10^{-4}$ – $2.0 \times 10^{-4}$   $ppb \cdot s^{-1}$ ), whereas SJZ\_LC, likely influenced by  
636 local emissions and complex topography, exhibits slightly lower peaks ( $1.0 \times 10^{-4}$ –  
637  $1.5 \times 10^{-4}$   $ppb \cdot s^{-1}$ ). SXU reaches  $\sim 1.7 \times 10^{-4}$   $ppb \cdot s^{-1}$ . At all these sites,  $P(OH)O_3$   
638 decreases with altitude and generally falls below  $1.0 \times 10^{-4}$   $ppb \cdot s^{-1}$  above 1 km. East  
639 China stations (TS, NUIST, LA, HNU, AHU, and CF) display similar peak timing  
640 (12:00–14:00), with near-surface maxima of  $1.0 \times 10^{-4}$ – $1.8 \times 10^{-4}$   $ppb \cdot s^{-1}$ . TS, NUIST,  
641 HNU, AHU, and CF reach  $\sim 1.5 \times 10^{-4}$ – $1.8 \times 10^{-4}$   $ppb \cdot s^{-1}$ , while LA peaks at  $\sim 1.4 \times 10^{-4}$   
642  $ppb \cdot s^{-1}$ . In South China (GIG, SUST, GZ\_ZL, GZ\_NS, GZ\_TM, GZ\_GY, and  
643 GZ\_DXC), the maxima occur slightly later (13:00–15:00) and are generally higher  
644 ( $1.3 \times 10^{-4}$ – $1.7 \times 10^{-4}$   $ppb \cdot s^{-1}$ ), with GZ\_GY reaching  $\sim 1.9 \times 10^{-4}$   $ppb \cdot s^{-1}$  and GZ\_NS,  
645 GZ\_TM, and GZ\_DXC  $\sim 1.8 \times 10^{-4}$   $ppb \cdot s^{-1}$ . Southwest China (CDAES and CQ) shows  
646 peaks of  $\sim 1.5 \times 10^{-4}$ – $2.5 \times 10^{-4}$   $ppb \cdot s^{-1}$ , including  $\sim 1.9 \times 10^{-4}$   $ppb \cdot s^{-1}$  at CQ and  
647  $\sim 1.5 \times 10^{-4}$   $ppb \cdot s^{-1}$  at CDAES. The Central China site LY exhibits a peak of  $\sim 1.5 \times 10^{-4}$   
648  $ppb \cdot s^{-1}$ , comparable to those in North and East China, indicating broadly similar  
649 ozone photochemical efficiencies across these regions.



650

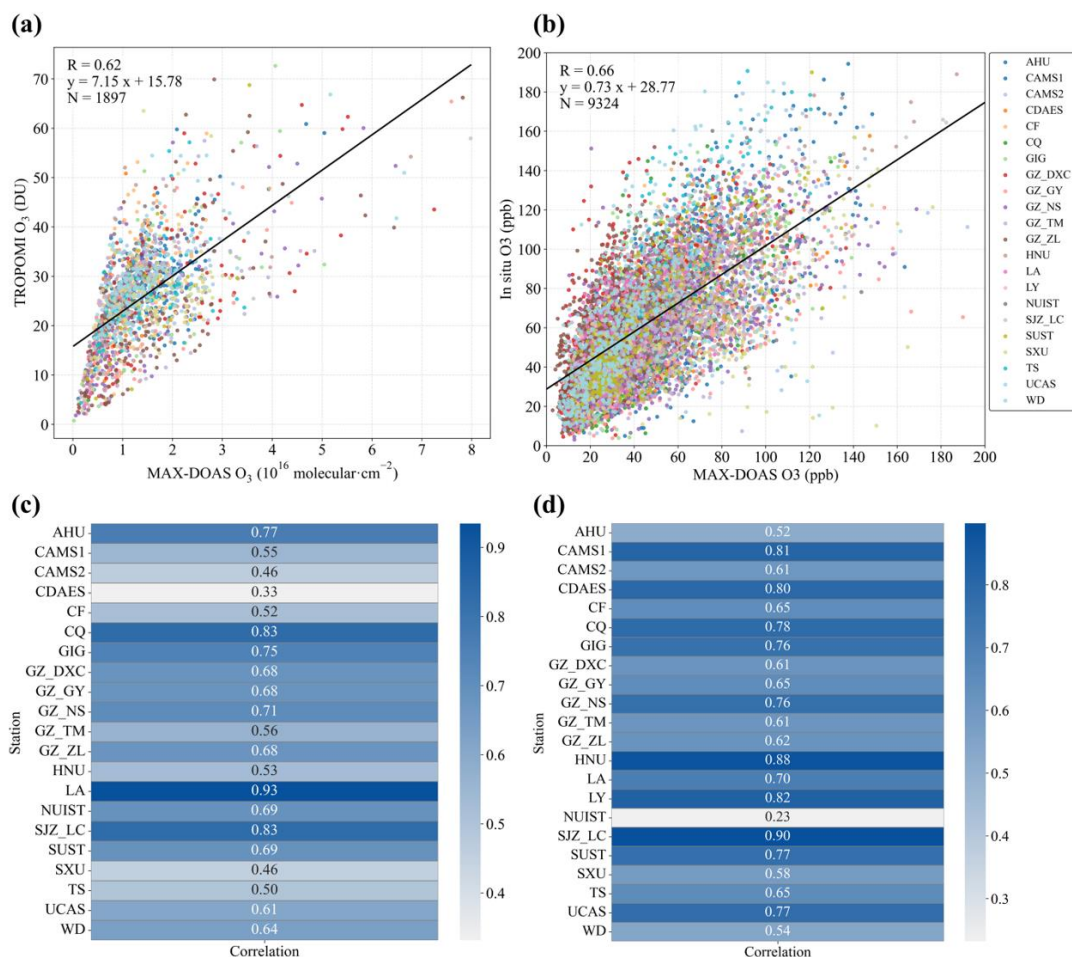
651 Figure 10. Mean vertical profiles of OH radicals produced by O<sub>3</sub> photolysis.

652

### 653 3.4 Validations with independent data

654 The dataset was validated using two independent approaches. First, O<sub>3</sub> VCD  
 655 retrieved from the MAX-DOAS network for 2021–2024 were evaluated against  
 656 coincident TROPOMI satellite observations. MAX-DOAS measurements were  
 657 averaged within ±30 min of the TROPOMI overpass (13:30–14:00 Beijing Time), and  
 658 TROPOMI pixels were spatially averaged over a 7 km × 5.5 km area center on each  
 659 site, consistent with the native spatial resolution of TROPOMI. As shown in Figure  
 660 11a, the two datasets exhibit a strong linear relationship, with a Pearson correlation  
 661 coefficient of  $R = 0.62$  ( $N = 1897$ ); site-resolved correlations are given in Figure 11c.  
 662 Second, near-surface O<sub>3</sub> concentrations retrieved at the 22 hyperspectral sites were  
 663 compared with in situ measurements from the nearest CNEMC over the same period.  
 664 Site pairs were selected following the spatial representativeness criteria of Song et al.  
 665 (2023b), Specifically, we prioritized the nearest CNEMC station within a maximum  
 666 distance of ~10–15 km (detailed in Table S1) and verified environmental consistency  
 667 between the paired sites using land-use and satellite-derived products, ensuring that

668 both sites sampled comparable urban or suburban atmospheric conditions. The  
 669 comparison (Figure 11b) shows a significant positive correlation ( $R = 0.66$ ,  $N = 9324$ ),  
 670 demonstrating good consistency between MAX-DOAS-derived surface  $O_3$  and  
 671 ground-based observations. The correlations for each hyperspectral site and its nearest  
 672 CNEMC are summarized in Figure 11d. Together, these two independent validations  
 673 demonstrate reasonable consistency and provide confidence in the dataset used in this  
 674 study.



675  
 676 Figure 11. (a) Correlation between  $O_3$  column densities retrieved from hyperspectral  
 677 ground-based stations and TROPOMI satellite observations; (b) correlation between  
 678 hyperspectral  $O_3$  column densities and in situ  $O_3$  measurements from the nearest  
 679 CNEMC; (c) site-specific correlations between hyperspectral and TROPOMI  $O_3$   
 680 column densities; (d) site-specific correlations between hyperspectral  $O_3$  column  
 681 densities and in situ  $O_3$  at the nearest CNEMC.

682

#### 683 4. Data availability

684 The vertical profiles of HONO and  $O_3$ , and the vertical profiles of OH radicals  
 685 over the major regions of China presented in this study, are freely available in .xlsx  
 686 format at Zenodo (<https://doi.org/10.5281/zenodo.18489836>; Zou et al., 2026).

687

## 688 5. Summary

689 We developed and released a comprehensive dataset of vertical profiles of  
690 HONO and O<sub>3</sub>, and the associated OH radical production rates, P(OH)<sub>HONO</sub> and  
691 P(OH)<sub>O<sub>3</sub></sub>, derived from the Chinese hyperspectral vertical remote-sensing network for  
692 2021–2024. The dataset spans 22 representative sites across North, East, Central,  
693 South, and Southwest China, covering a wide range of climatic regimes and surface  
694 types, and represents one of the most extensive publicly available collections in China  
695 in terms of spatial coverage and vertical resolution of photochemical parameters  
696 relevant to OH precursors. Independent validation against TROPOMI satellite  
697 retrievals and in situ measurements from the CNEMC demonstrates robust  
698 consistency. Mean diurnal profiles within 0–4 km reveal pronounced regional and  
699 vertical contrasts in HONO and O<sub>3</sub> driven photochemistry. Both J(HONO) and  
700 J(O(<sup>1</sup>D)) exhibit radiation controlled, single-peaked diurnal cycles, with maxima  
701 around local noon (11:00–14:00), and remain elevated in the upper mixed layer and  
702 the lower free troposphere, reflecting the combined effects of radiative transfer and  
703 aerosol extinction on the vertical distribution of photolysis rates. Accordingly,  
704 P(OH)<sub>HONO</sub> and P(OH)<sub>O<sub>3</sub></sub> peak near the surface and decrease with height, indicating  
705 that the boundary layer is the primary daytime source region of OH. At several  
706 plateau and mountainous sites, however, the lower free troposphere also shows a  
707 substantial radical production potential. Urban and highly industrialized sites exhibit  
708 higher photolysis rates and OH production, reflecting the combined effects of high  
709 precursor concentrations and strong radiation, while high-altitude clean-background  
710 sites, despite lower near-surface concentrations, maintain relatively large photolysis  
711 rates and significant OH production at middle and upper levels due to weaker aerosol  
712 extinction and stronger shortwave radiation, showing a vertical photochemical  
713 structure distinct from that over plains.

714 With continuous temporal coverage ranging from five months to 3.5 years and  
715 multi-site vertical profiling, this dataset provides a valuable foundation for: (1)  
716 quantifying the relative contributions of HONO and O<sub>3</sub> photolysis to the OH budget  
717 in the boundary layer and the lower free troposphere; (2) constraining radical initial  
718 conditions and radiative parameterizations in regional and global chemical transport  
719 models; (3) enabling cross-validation and synergistic inversion among ground-based,  
720 UAV, and satellite observations; (4) advancing studies of photochemical pollution  
721 formation, secondary aerosol production, and atmospheric oxidation capacity; and (5)  
722 supporting air-quality management and policy development as a complementary  
723 national monitoring resource. (6) serving as a critical benchmark for assessing and  
724 reducing uncertainties in vertical parameterization schemes (e.g., turbulent mixing,  
725 photolysis rates, heterogeneous reactions) within atmospheric chemical transport  
726 models. However, it is important to note the limitations of the current dataset. The  
727 time span (2021–2024) limits the capacity for robust analysis of long-term interannual  
728 trends driven by climate change or policy shifts. The observed photochemical regimes  
729 may not fully represent conditions during extreme climatic years outside this period,

730 and the climatological representativeness of sites with shorter operational histories  
731 requires continued data accumulation.

732

### 733 **Financial support**

734 This work was supported by the National Natural Science Foundation of China  
735 (42588301, 42225504), the President's Foundation of Hefei Institutes of Physical  
736 Science, Chinese Academy of Sciences (YZJJQY202401, BJPY2024B09).

737

### 738 **References**

739 Aliwell, S. R., Van Roozendaal, M., Johnston, P. V., Richter, A., Wagner, T.,  
740 Arlander, D. W., Burrows, J. P., Fish, D. J., Jones, R. L., Tørnkvist, K. K.,  
741 Lambert, J.-C., Pfeilsticker, K., and Pundt, I.: Analysis for BrO in zenith-sky  
742 spectra: An intercomparison exercise for analysis improvement, *Journal of*  
743 *Geophysical Research: Atmospheres*, 107, ACH 10-1-ACH 10-20,  
744 <https://doi.org/10.1029/2001JD000329>, 2002.

745 Ancellet, G., Viatte, C., Boynard, A., Ravetta, F., Pelon, J., Cailteau-Fischbach, C.,  
746 Genau, P., Capo, J., Roy, A., and Nédélec, P.: Analysis of the day-to-day  
747 variability of ozone vertical profiles in the lower troposphere during the 2022  
748 Paris ACROSS campaign, *Atmospheric Chemistry and Physics*, 24, 12963–  
749 12983, <https://doi.org/10.5194/acp-24-12963-2024>, 2024.

750 Andersen, S. T., Carpenter, L. J., Reed, C., Lee, J. D., Chance, R., Sherwen, T.,  
751 Vaughan, A. R., Stewart, J., Edwards, P. M., Bloss, W. J., Sommariva, R.,  
752 Crilley, L. R., Nott, G. J., Neves, L., Read, K., Heard, D. E., Seakins, P. W.,  
753 Whalley, L. K., Boustead, G. A., Fleming, L. T., Stone, D., and Fomba, K. W.:  
754 Extensive field evidence for the release of HONO from the photolysis of nitrate  
755 aerosols, *Science Advances*, 9, eadd6266,  
756 <https://doi.org/10.1126/sciadv.add6266>, 2023.

757 Anon: Systematic Evaluation of Four Satellite AOD Datasets for Estimating PM2.5  
758 Using a Random Forest Approach, *Remote sensing*, 15, 2064–2064,  
759 <https://doi.org/10.3390/rs15082064>, 2023.

760 Aumont, B., Chervier, F., and Laval, S.: Contribution of HONO sources to the  
761 NOx/HOx/O3 chemistry in the polluted boundary layer, *Atmospheric*  
762 *Environment*, 37, 487–498, [https://doi.org/10.1016/S1352-2310\(02\)00920-2](https://doi.org/10.1016/S1352-2310(02)00920-2),  
763 2003.

764 Chambers, S. D., Guérette, E.-A., Monk, K., Griffiths, A. D., Zhang, Y., Duc, H.,  
765 Cope, M., Emmerson, K. M., Chang, L. T., Silver, J. D., Utembe, S., Crawford,  
766 J., Williams, A. G., and Keywood, M.: Skill-Testing Chemical Transport Models  
767 across Contrasting Atmospheric Mixing States Using Radon-222, *Atmosphere*,  
768 10, 25, <https://doi.org/10.3390/atmos10010025>, 2019.

- 769 Chen, Z., Xie, Y., Liu, J., Shen, L., Cheng, X., Han, H., Yang, M., Shen, Y., Zhao, T.,  
770 and Hu, J.: Distinct seasonality in vertical variations of tropospheric ozone over  
771 coastal regions of southern China, *Science of The Total Environment*, 874,  
772 162423, <https://doi.org/10.1016/j.scitotenv.2023.162423>, 2023.
- 773 Chen, Z., Liu, R., Wu, S., Xu, J., Wu, Y., and Qi, S.: Diurnal variation characteristics  
774 and meteorological causes of autumn ozone in the Pearl River Delta, China,  
775 *Science of The Total Environment*, 908, 168469,  
776 <https://doi.org/10.1016/j.scitotenv.2023.168469>, 2024.
- 777 Couillard, M. H., Schwab, M. J., Schwab, J. J., Lu, C.-H. (Sarah), Joseph, E., Stutsrim,  
778 B., Shrestha, B., Zhang, J., Knepp, T. N., and Gronoff, G. P.: Vertical Profiles of  
779 Ozone Concentrations in the Lower Troposphere Downwind of New York City  
780 During LISTOS 2018–2019, *Journal of Geophysical Research: Atmospheres*,  
781 126, e2021JD035108, <https://doi.org/10.1029/2021JD035108>, 2021.
- 782 David, L. M. and Nair, P. R.: Diurnal and seasonal variability of surface ozone and  
783 NO<sub>x</sub> at a tropical coastal site: Association with mesoscale and synoptic  
784 meteorological conditions, *Journal of Geophysical Research: Atmospheres*, 116,  
785 <https://doi.org/10.1029/2010JD015076>, 2011.
- 786 Dewan, S. and Lakhani, A.: Tropospheric ozone and its natural precursors impacted  
787 by climatic changes in emission and dynamics, *Front. Environ. Sci.*, 10,  
788 <https://doi.org/10.3389/fenvs.2022.1007942>, 2022.
- 789 Donzelli, G. and Suarez-Varela, M. M.: Tropospheric Ozone: A Critical Review of  
790 the Literature on Emissions, Exposure, and Health Effects, *Atmosphere*, 15, 779,  
791 <https://doi.org/10.3390/atmos15070779>, 2024.
- 792 Elshorbany, Y., Barnes, I., Becker, K., Kleffmann, J., and Wiesen, P.: Sources and  
793 cycling of tropospheric hydroxyl radicals - An overview, *USF St. Petersburg*  
794 *Campus Faculty Publications*, 2010.
- 795 Fardilah, R. D., Turyanti, A., Pangestu, L. A., Dominica, M. V., and Perdinan:  
796 Systematic Literature Review on Ozone Dispersion Correlated with Diurnal  
797 Concentration Pattern in Urban and Rural Areas, *Agromet*, 37, 77–90,  
798 <https://doi.org/10.29244/j.agromet.37.2.77-90>, 2023.
- 799 Fleischmann, O. C., Hartmann, M., Burrows, J. P., and Orphal, J.: New ultraviolet  
800 absorption cross-sections of BrO at atmospheric temperatures measured by time-  
801 windowing Fourier transform spectroscopy, *Journal of Photochemistry and*  
802 *Photobiology A: Chemistry*, 168, 117–132,  
803 <https://doi.org/10.1016/j.jphotochem.2004.03.026>, 2004.
- 804 Garcia-Nieto, D., Benavent, N., and Saiz-Lopez, A.: Measurements of atmospheric  
805 HONO vertical distribution and temporal evolution in Madrid (Spain) using the  
806 MAX-DOAS technique, *Science of The Total Environment*, 643, 957–966,

807 <https://doi.org/10.1016/j.scitotenv.2018.06.180>, 2018b.

808 Gu, R., Shen, H., Xue, L., Wang, T., Gao, J., Li, H., Liang, Y., Xia, M., Yu, C., Liu,  
809 Y., and Wang, W.: Investigating the sources of atmospheric nitrous acid (HONO)  
810 in the megacity of Beijing, China, *Science of The Total Environment*, 812,  
811 152270, <https://doi.org/10.1016/j.scitotenv.2021.152270>, 2022.

812 Guo, J., Zhang, X., Gao, Y., Wang, Z., Zhang, M., Xue, W., Herrmann, H., Brasseur,  
813 G. P., Wang, T., and Wang, Z.: Evolution of Ozone Pollution in China: What  
814 Track Will It Follow?, *Environ. Sci. Technol.*, 57, 109–117,  
815 <https://doi.org/10.1021/acs.est.2c08205>, 2023.

816 Guo, P., Su, Y., Sun, X., Liu, C., Cui, B., Xu, X., Ouyang, Z., and Wang, X.: Urban–  
817 Rural Comparisons of Biogenic Volatile Organic Compounds and Ground-Level  
818 Ozone in Beijing, *Forests*, 15, 508, <https://doi.org/10.3390/fl15030508>, 2024a.

819 Guo, W., Yang, Y., Zhang, J., Han, K., Yang, Y., Chen, Q., Li, S., and Zhu, Y.:  
820 Effects of valley topography on ozone pollution in the Lanzhou valley: A  
821 numerical case study, *Environ Pollut*, 363, 125225,  
822 <https://doi.org/10.1016/j.envpol.2024.125225>, 2024b.

823 Hao, Q., Jiang, N., Zhang, R., Yang, L., and Li, S.: Characteristics, sources, and  
824 reactions of nitrous acid during winter at an urban site in the Central Plains  
825 Economic Region in China, *Atmospheric Chemistry and Physics*, 20, 7087–7102,  
826 <https://doi.org/10.5194/acp-20-7087-2020>, 2020.

827 He, C., Wu, Q., Li, B., Liu, J., Gong, X., and Zhang, L.: Surface ozone pollution in  
828 China: Trends, exposure risks, and drivers, *Front. Public Health*, 11,  
829 <https://doi.org/10.3389/fpubh.2023.1131753>, 2023a.

830 He, G., He, C., Wang, H., Lu, X., Pei, C., Qiu, X., Liu, C., Wang, Y., Liu, N., Zhang,  
831 J., Lei, L., Liu, Y., Wang, H., Deng, T., Fan, Q., and Fan, S.: Nighttime ozone in  
832 the lower boundary layer: insights from 3-year tower-based measurements in  
833 South China and regional air quality modeling, *Atmospheric Chemistry and  
834 Physics*, 23, 13107–13124, <https://doi.org/10.5194/acp-23-13107-2023>, 2023b.

835 He, S., Wang, S., Zhang, S., Zhu, J., Sun, Z., Xue, R., and Zhou, B.: Vertical  
836 distributions of atmospheric HONO and the corresponding OH radical  
837 production by photolysis at the suburb area of Shanghai, China, *Science of The  
838 Total Environment*, 858, 159703,  
839 <https://doi.org/10.1016/j.scitotenv.2022.159703>, 2023c.

840 He, Y., Wang, H., Wang, H., Xu, X., Li, Y., and Fan, S.: Meteorology and  
841 topographic influences on nocturnal ozone increase during the summertime over  
842 Shaoguan, China, *Atmospheric Environment*, 256, 118459,  
843 <https://doi.org/10.1016/j.atmosenv.2021.118459>, 2021.

- 844 Hu, Q., Ji, X., Hong, Q., Li, J., Li, Q., Ou, J., Liu, H., Xing, C., Tan, W., Chen, J.,  
845 Chang, B., and Liu, C.: Vertical Evolution of Ozone Formation Sensitivity Based  
846 on Synchronous Vertical Observations of Ozone and Proxies for Its Precursors:  
847 Implications for Ozone Pollution Prevention Strategies, *Environ Sci Technol*, 58,  
848 4291–4301, <https://doi.org/10.1021/acs.est.4c00637>, 2024.
- 849 Itahashi, S., Mathur, R., Hogrefe, C., and Zhang, Y.: Modeling stratospheric intrusion  
850 and trans-Pacific transport on tropospheric ozone using hemispheric CMAQ  
851 during April 2010 – Part 1: Model evaluation and air mass characterization for  
852 stratosphere–troposphere transport, *Atmospheric Chemistry and Physics*, 20,  
853 3373–3396, <https://doi.org/10.5194/acp-20-3373-2020>, 2020.
- 854 Ji, X., Liu, C., Wang, Y., Hu, Q., Lin, H., Zhao, F., Xing, C., Tang, G., Zhang, J., and  
855 Wagner, T.: Ozone profiles without blind area retrieved from MAX-DOAS  
856 measurements and comprehensive validation with multi-platform observations,  
857 *Remote Sensing of Environment*, 284, 113339,  
858 <https://doi.org/10.1016/j.rse.2022.113339>, 2023.
- 859 Johnson, M. S., Rozanov, A., Weber, M., Mettig, N., Sullivan, J., Newchurch, M. J.,  
860 Kuang, S., Leblanc, T., Chouza, F., Berkoff, T. A., Gronoff, G., Strawbridge, K.  
861 B., Alvarez, R. J., Langford, A. O., Senff, C. J., Kirgis, G., McCarty, B., and  
862 Twigg, L.: TOLNet validation of satellite ozone profiles in the troposphere:  
863 impact of retrieval wavelengths, *Atmospheric Measurement Techniques*, 17,  
864 2559–2582, <https://doi.org/10.5194/amt-17-2559-2024>, 2024.
- 865 Kim, H., Park, R. J., Hong, S.-Y., Park, D.-H., Kim, S.-W., Oak, Y. J., Feng, X., Lin,  
866 H., and Fu, T.-M.: A mixed layer height parameterization in a 3-D chemical  
867 transport model: Implications for gas and aerosol simulations, *Sci Total Environ*,  
868 955, 176838, <https://doi.org/10.1016/j.scitotenv.2024.176838>, 2024.
- 869 Li, K., Jacob, D. J., Shen, L., Lu, X., De Smedt, I., and Liao, H.: Increases in surface  
870 ozone pollution in China from 2013 to 2019: anthropogenic and meteorological  
871 influences, *Atmospheric Chemistry and Physics*, 20, 11423–11433,  
872 <https://doi.org/10.5194/acp-20-11423-2020>, 2020.
- 873 Li, K., Tan, R., Qiao, W., Lee, T., Wang, Y., Zhang, D., Tang, M., Zhao, W., Gu, Y.,  
874 Fan, S., Zhang, J., Lyu, X., Xue, L., Xu, J., Ma, Z., Latif, M. T., Amnuaylojaroen,  
875 T., Gil, J., Lee, M.-H., Bak, J., Kim, J., Liao, H., Kanaya, Y., Lu, X., Nagashima,  
876 T., and Koo, J.-H.: Surface and tropospheric ozone over East Asia and Southeast  
877 Asia from observations: distributions, trends, and variability, *Atmospheric  
878 Chemistry and Physics*, 25, 11575–11596, [https://doi.org/10.5194/acp-25-11575-  
879 2025](https://doi.org/10.5194/acp-25-11575-2025), 2025a.
- 880 Li, M., McDonald, B. C., McKeen, S. A., Eskes, H., Levelt, P., Francoeur, C.,  
881 Harkins, C., He, J., Barth, M., Henze, D. K., Bela, M. M., Trainer, M., de Gouw,  
882 J. A., and Frost, G. J.: Assessment of Updated Fuel-Based Emissions Inventories

883 Over the Contiguous United States Using TROPOMI NO<sub>2</sub> Retrievals, *Journal of*  
884 *Geophysical Research: Atmospheres*, 126, e2021JD035484,  
885 <https://doi.org/10.1029/2021JD035484>, 2021.

886 Li, Y., Xing, C., Peng, H., Jiao, P., Zhang, Q., Liu, C., Sun, Z., Tan, W., and Liu, C.:  
887 Vertical Differences in NO<sub>2</sub>-to-HONO Heterogeneous Conversion and HONO-  
888 Driven OH Production over Inland, Coastal, and Island Regions, *Environ. Sci.*  
889 *Technol.*, 59, 26020–26030, <https://doi.org/10.1021/acs.est.5c10318>, 2025b.

890 Liang, Y., Zha, Q., Wang, W., Cui, L., Lui, K. H., Ho, K. F., Wang, Z., Lee, S., and  
891 Wang, T.: Revisiting nitrous acid (HONO) emission from on-road vehicles: A  
892 tunnel study with a mixed fleet, *Journal of the Air & Waste Management*  
893 *Association*, 67, 797–805, <https://doi.org/10.1080/10962247.2017.1293573>,  
894 2017.

895 Liao, Z., Pan, Y., Ma, P., Jia, X., Cheng, Z., Wang, Q., Dou, Y., Zhao, X., Zhang, J.,  
896 and Quan, J.: Meteorological and chemical controls on surface ozone diurnal  
897 variability in Beijing: A clustering-based perspective, *Atmospheric Environment*,  
898 295, 119566, <https://doi.org/10.1016/j.atmosenv.2022.119566>, 2023.

899 Liao, Z., Gao, M., Zhang, J., Sun, J., Quan, J., Jia, X., Pan, Y., and Fan, S.: Mixing-  
900 layer-height-referenced ozone vertical distribution in the lower troposphere of  
901 Chinese megacities: stratification, classification, and meteorological and  
902 photochemical mechanisms, *Atmospheric Chemistry and Physics*, 24, 3541–  
903 3557, <https://doi.org/10.5194/acp-24-3541-2024>, 2024.

904 Liao, Z., Zhang, J., Gao, M., and Ma, Z.: Widespread stratospheric intrusion influence  
905 on summer ozone pollution over China revealed by multi-site ozonesonde and  
906 validated EAC4 reanalysis, *Atmospheric Chemistry and Physics*, 25, 14865–  
907 14877, <https://doi.org/10.5194/acp-25-14865-2025>, 2025.

908 Lin, H., Xing, C., Hong, Q., Liu, C., Ji, X., Liu, T., Lin, J., Lu, C., Tan, W., Li, Q.,  
909 and Liu, H.: Diagnosis of Ozone Formation Sensitivities in Different Height  
910 Layers via MAX-DOAS Observations in Guangzhou, *Journal of Geophysical*  
911 *Research: Atmospheres*, 127, e2022JD036803,  
912 <https://doi.org/10.1029/2022JD036803>, 2022.

913 Liu, C., Xing, C., Hu, Q., Li, Q., Liu, H., Hong, Q., Tan, W., Ji, X., Lin, H., Lu, C.,  
914 Lin, J., Liu, H., Wei, S., Chen, J., Yang, K., Wang, S., Liu, T., and Chen, Y.:  
915 Ground-Based Hyperspectral Stereoscopic Remote Sensing Network: A  
916 Promising Strategy to Learn Coordinated Control of O<sub>3</sub> and PM<sub>2.5</sub> over China,  
917 *Engineering*, 19, 71–83, <https://doi.org/10.1016/j.eng.2021.02.019>, 2022a.

918 Liu, H., Han, X., Tang, G., Zhang, J., Xia, X., Zhang, M., and Meng, L.: Model  
919 analysis of vertical exchange of boundary layer ozone and its impact on surface  
920 air quality over the North China Plain, *Science of The Total Environment*, 821,

- 921 153436, <https://doi.org/10.1016/j.scitotenv.2022.153436>, 2022b.
- 922 Liu, P., Xue, C., Ye, C., Liu, C., Zhang, C., Wang, J., Zhang, Y., Liu, J., and Mu, Y.:  
923 The Lack of HONO Measurement May Affect the Accurate Diagnosis of Ozone  
924 Production Sensitivity, *ACS Environ. Au*, 3, 18–23,  
925 <https://doi.org/10.1021/acsenvironau.2c00048>, 2023a.
- 926 Liu, X., Yi, G., Zhou, X., Zhang, T., Bie, X., Li, J., and Tan, H.: Spatio-temporal  
927 variations of PM<sub>2.5</sub> and O<sub>3</sub> in China during 2013–2021: Impact factor analysis,  
928 *Environmental Pollution*, 334, 122189,  
929 <https://doi.org/10.1016/j.envpol.2023.122189>, 2023b.
- 930 Lu, Y., Kong, L., Shen, J., Liu, B., An, Y., Wang, Y., Tan, J., and Wang, L.:  
931 Characteristics and influencing factors of ambient ozone pollution in Hangzhou  
932 in the relative humidity range with high ozone levels, *Atmospheric Pollution*  
933 *Research*, 16, 102648, <https://doi.org/10.1016/j.apr.2025.102648>, 2025.
- 934 Lyu, Y., Xu, H., Wu, H., Han, F., Lv, F., Kang, A., and Pang, X.: Spatiotemporal  
935 variations of PM<sub>2.5</sub> and ozone in urban agglomerations of China and  
936 meteorological drivers for ozone using explainable machine learning,  
937 *Environmental Pollution*, 365, 125380,  
938 <https://doi.org/10.1016/j.envpol.2024.125380>, 2025.
- 939 Meng, F., Qin, M., Tang, K., Duan, J., Fang, W., Liang, S., Ye, K., Xie, P., Sun, Y.,  
940 Xie, C., Ye, C., Fu, P., Liu, J., and Liu, W.: High-resolution vertical distribution  
941 and sources of HONO and NO<sub>2</sub> in the nocturnal boundary layer in urban Beijing,  
942 China, *Atmospheric Chemistry and Physics*, 20, 5071–5092,  
943 <https://doi.org/10.5194/acp-20-5071-2020>, 2020.
- 944 Monks, P. S., Archibald, A. T., Colette, A., Cooper, O., Coyle, M., Derwent, R.,  
945 Fowler, D., Granier, C., Law, K. S., Mills, G. E., Stevenson, D. S., Tarasova, O.,  
946 Thouret, V., von Schneidmesser, E., Sommariva, R., Wild, O., and Williams, M.  
947 L.: Tropospheric ozone and its precursors from the urban to the global scale from  
948 air quality to short-lived climate forcer, *Atmospheric Chemistry and Physics*, 15,  
949 8889–8973, <https://doi.org/10.5194/acp-15-8889-2015>, 2015.
- 950 Orphal, J. and Chance, K.: Ultraviolet and visible absorption cross-sections for  
951 HITRAN, *Journal of Quantitative Spectroscopy and Radiative Transfer*, 82, 491–  
952 504, [https://doi.org/10.1016/S0022-4073\(03\)00173-0](https://doi.org/10.1016/S0022-4073(03)00173-0), 2003.
- 953 Park, S., Son, S.-W., Jung, M.-I., Park, J., and Park, S. S.: Evaluation of tropospheric  
954 ozone reanalyses with independent ozonesonde observations in East Asia, *Geosci.*  
955 *Lett.*, 7, 12, <https://doi.org/10.1186/s40562-020-00161-9>, 2020.
- 956 Qiao, X., Guo, H., Wang, P., Tang, Y., Ying, Q., Zhao, X., Deng, W., and Zhang, H.:  
957 Fine Particulate Matter and Ozone Pollution in the 18 Cities of the Sichuan Basin  
958 in Southwestern China: Model Performance and Characteristics, *Aerosol Air*

959 Qual. Res., 19, 2308–2319, <https://doi.org/10.4209/aaqr.2019.05.0235>, 2019.

960 Qiu, Y., Li, X., Chai, W., Liu, Y., Song, M., Tian, X., Zou, Q., Lou, W., Zhang, W.,  
961 Li, J., and Zhang, Y.: Insights into ozone pollution control in urban areas by  
962 decoupling meteorological factors based on machine learning, *Atmospheric*  
963 *Chemistry and Physics*, 25, 1749–1763, [https://doi.org/10.5194/acp-25-1749-](https://doi.org/10.5194/acp-25-1749-2025)  
964 2025, 2025.

965 Qu, H., Wang, Y., Zhang, R., and Li, J.: Extending Ozone-Precursor Relationships in  
966 China From Peak Concentration to Peak Time, *Journal of Geophysical Research:*  
967 *Atmospheres*, 125, e2020JD033670, <https://doi.org/10.1029/2020JD033670>,  
968 2020.

969 R. Crilley, L., Kramer, L., D. Pope, F., K. Whalley, L., R. Cryer, D., E. Heard, D.,  
970 D. Lee, J., Reed, C., and J. Bloss, W.: On the interpretation of in situ HONO  
971 observations via photochemical steady state, *Faraday Discussions*, 189, 191–212,  
972 <https://doi.org/10.1039/C5FD00224A>, 2016.

973 Ryan, R. G., Rhodes, S., Tully, M., Wilson, S., Jones, N., Frieß, U., and Schofield, R.:  
974 Daytime HONO, NO<sub>2</sub> and aerosol distributions from MAX-DOAS observations  
975 in Melbourne, *Atmospheric Chemistry and Physics*, 18, 13969–13985,  
976 <https://doi.org/10.5194/acp-18-13969-2018>, 2018a.

977 Sekiya, T., Emili, E., Miyazaki, K., Inness, A., Qu, Z., Pierce, R. B., Jones, D.,  
978 Worden, H., Cheng, W. Y. Y., Huijnen, V., and Koren, G.: Assessing the relative  
979 impacts of satellite ozone and its precursor observations to improve global  
980 tropospheric ozone analysis using multiple chemical reanalysis systems,  
981 *Atmospheric Chemistry and Physics*, 25, 2243–2268,  
982 <https://doi.org/10.5194/acp-25-2243-2025>, 2025.

983 Serdyuchenko, A., Gorshelev, V., Weber, M., Chehade, W., and Burrows, J. P.: High  
984 spectral resolution ozone absorption cross-sections &ndash; Part 2: Temperature  
985 dependence, *Atmospheric Measurement Techniques*, 7, 625–636,  
986 <https://doi.org/10.5194/amt-7-625-2014>, 2014.

987 Sharma, B. R., Kuttippurath, J., and Gopikrishnan, G. S.: Tropospheric ozone as an  
988 atmospheric pollutant and short-lived climate forcer in the Third Pole,  
989 *Chemosphere*, 380, 144474, <https://doi.org/10.1016/j.chemosphere.2025.144474>,  
990 2025.

991 Shi, Y., Zeng, Q., Liu, L., Huo, J., Zhang, Z., Ding, W., and Hu, F.: Observed  
992 Evidence That Subsidence Process Stabilizes the Boundary Layer and Increases  
993 the Ground Concentration of Secondary Pollutants, *Journal of Geophysical*  
994 *Research: Atmospheres*, 127, e2021JD035244,  
995 <https://doi.org/10.1029/2021JD035244>, 2022.

996 Shu, Z., Zhao, T., Chen, Y., Liu, Y., Yang, F., Jiang, Y., He, G., Yang, Q., and Zhang,

- 997 Y.: Terrain effect on atmospheric process in seasonal ozone variation over the  
998 Sichuan Basin, Southwest China, *Environmental Pollution*, 338, 122622,  
999 <https://doi.org/10.1016/j.envpol.2023.122622>, 2023.
- 1000 Song, M., Zhao, X., Liu, P., Mu, J., He, G., Zhang, C., Tong, S., Xue, C., Zhao, X.,  
1001 Ge, M., and Mu, Y.: Atmospheric NO<sub>x</sub> oxidation as major sources for nitrous  
1002 acid (HONO), *npj Clim Atmos Sci*, 6, 30, [https://doi.org/10.1038/s41612-023-](https://doi.org/10.1038/s41612-023-00357-8)  
1003 00357-8, 2023a.
- 1004 Song, X., Li, X.-B., Yuan, B., He, X., Chen, Y., Wang, S., Huangfu, Y., Peng, Y.,  
1005 Zhang, C., Liu, A., Yang, H., Liu, C., Li, J., and Shao, M.: Elucidating key  
1006 factors in regulating budgets of ozone and its precursors in atmospheric  
1007 boundary layer, *npj Clim Atmos Sci*, 7, 262, [https://doi.org/10.1038/s41612-024-](https://doi.org/10.1038/s41612-024-00818-8)  
1008 00818-8, 2024.
- 1009 Song, Y., Xing, C., Liu, C., Lin, J., Wu, H., Liu, T., Lin, H., Zhang, C., Tan, W., Ji,  
1010 X., Liu, H., and Li, Q.: Evaluation of transport processes over North China Plain  
1011 and Yangtze River Delta using MAX-DOAS observations, *Atmospheric*  
1012 *Chemistry and Physics*, 23, 1803–1824, [https://doi.org/10.5194/acp-23-1803-](https://doi.org/10.5194/acp-23-1803-2023)  
1013 2023, 2023b.
- 1014 Song, Y., Wang, P., Yang, Y., Tang, J., and Liao, H.: Meteorological conditions and  
1015 physicochemical processes amplifying ozone pollution during heatwaves in  
1016 major city clusters of China, *Atmospheric Research*, 330, 108580,  
1017 <https://doi.org/10.1016/j.atmosres.2025.108580>, 2026.
- 1018 Spataro, F. and Ianniello, A.: Sources of atmospheric nitrous acid: State of the science,  
1019 current research needs, and future prospects, *Journal of the Air & Waste*  
1020 *Management Association*, 64, 1232–1250,  
1021 <https://doi.org/10.1080/10962247.2014.952846>, 2014.
- 1022 Spurr, R. J. D.: VLIDORT: A linearized pseudo-spherical vector discrete ordinate  
1023 radiative transfer code for forward model and retrieval studies in multilayer  
1024 multiple scattering media, *Journal of Quantitative Spectroscopy and Radiative*  
1025 *Transfer*, 102, 316–342, <https://doi.org/10.1016/j.jqsrt.2006.05.005>, 2006.
- 1026 Stutz, J., Kim, E. S., Platt, U., Bruno, P., Perrino, C., and Febo, A.: UV-visible  
1027 absorption cross sections of nitrous acid, *Journal of Geophysical Research:*  
1028 *Atmospheres*, 105, 14585–14592, <https://doi.org/10.1029/2000JD900003>, 2000.
- 1029 Su, W., Liu, C., Hu, Q., Fan, G., Xie, Z., Huang, X., Zhang, T., Chen, Z., Dong, Y., Ji,  
1030 X., Liu, H., Wang, Z., and Liu, J.: Characterization of ozone in the lower  
1031 troposphere during the 2016 G20 conference in Hangzhou, *Sci Rep*, 7, 17368,  
1032 <https://doi.org/10.1038/s41598-017-17646-x>, 2017.
- 1033 Tang, Y., An, J., Wang, F., Li, Y., Qu, Y., Chen, Y., and Lin, J.: Impacts of an  
1034 unknown daytime HONO source on the mixing ratio and budget of HONO, and

- 1035 hydroxyl, hydroperoxyl, and organic peroxy radicals, in the coastal regions of  
1036 China, *Atmospheric Chemistry and Physics*, 15, 9381–9398,  
1037 <https://doi.org/10.5194/acp-15-9381-2015>, 2015.
- 1038 Thalman, R. and Volkamer, R.: Temperature dependent absorption cross-sections of  
1039 O<sub>2</sub>–O<sub>2</sub> collision pairs between 340 and 630 nm and at atmospherically relevant  
1040 pressure, *Phys. Chem. Chem. Phys.*, 15, 15371,  
1041 <https://doi.org/10.1039/c3cp50968k>, 2013.
- 1042 Thürkow, M., Schaap, M., Kranenburg, R., Pfäfflin, F., Neunhäuserer, L., Wolke, R.,  
1043 Heinold, B., Stoll, J., Lupaşcu, A., Nordmann, S., Minkos, A., and Butler, T.:  
1044 Dynamic evaluation of modeled ozone concentrations in Germany with four  
1045 chemistry transport models, *Science of The Total Environment*, 906, 167665,  
1046 <https://doi.org/10.1016/j.scitotenv.2023.167665>, 2024.
- 1047 Torres, O., Jethva, H., Ahn, C., Jaross, G., and Loyola, D. G.: TROPOMI aerosol  
1048 products: evaluation and observations of synoptic-scale carbonaceous aerosol  
1049 plumes during 2018–2020, *Atmospheric Measurement Techniques*, 13, 6789–  
1050 6806, <https://doi.org/10.5194/amt-13-6789-2020>, 2020b.
- 1051 Vandaele, A. C., Hermans, C., Simon, P. C., Carleer, M., Colin, R., Fally, S.,  
1052 Mérienne, M. F., Jenouvrier, A., and Coquart, B.: Measurements of the NO<sub>2</sub>  
1053 absorption cross-section from 42 000 cm<sup>-1</sup> to 10 000 cm<sup>-1</sup> (238–1000 nm) at  
1054 220 K and 294 K, *Journal of Quantitative Spectroscopy and Radiative Transfer*,  
1055 59, 171–184, [https://doi.org/10.1016/S0022-4073\(97\)00168-4](https://doi.org/10.1016/S0022-4073(97)00168-4), 1998.
- 1056 Wang, N., Du, Y., Chen, D., Meng, H., Chen, X., Zhou, L., Shi, G., Zhan, Y., Feng,  
1057 M., Li, W., Chen, M., Li, Z., and Yang, F.: Spatial disparities of ozone pollution  
1058 in the Sichuan Basin spurred by extreme, hot weather, *Atmospheric Chemistry  
1059 and Physics*, 24, 3029–3042, <https://doi.org/10.5194/acp-24-3029-2024>, 2024a.
- 1060 Wang, R., Shen, H., Zeng, C., Chen, J., Wang, Y., and Li, Y.: A global land daily 10-  
1061 km-resolution surface ozone dataset from 2013–2022, *Sci Data*, 12, 1710,  
1062 <https://doi.org/10.1038/s41597-025-05990-x>, 2025a.
- 1063 Wang, W.-N., Cheng, T.-H., Gu, X.-F., Chen, H., Guo, H., Wang, Y., Bao, F.-W., Shi,  
1064 S.-Y., Xu, B.-R., Zuo, X., Meng, C., and Zhang, X.-C.: Assessing Spatial and  
1065 Temporal Patterns of Observed Ground-level Ozone in China, *Sci Rep*, 7, 3651,  
1066 <https://doi.org/10.1038/s41598-017-03929-w>, 2017.
- 1067 Wang, X., Zhang, H., Hong, X., Xiang, Y., Wang, S., Zhang, T., Qin, Z., and Ou, J.:  
1068 Vertical profiles and regional transport of ozone in typical area of Yangtze-  
1069 Huaihe River Basin during the autumn base on multiple lidars, *Atmospheric  
1070 Pollution Research*, 15, 101983, <https://doi.org/10.1016/j.apr.2023.101983>,  
1071 2024b.
- 1072 Wang, Y., Puķite, J., Wagner, T., Donner, S., Beirle, S., Hilboll, A., Vrekoussis, M.,

- 1073 Richter, A., Apituley, A., Piters, A., Allaart, M., Eskes, H., Frumau, A., Van  
1074 Roozendael, M., Lampel, J., Platt, U., Schmitt, S., Swart, D., and Vonk, J.:  
1075 Vertical Profiles of Tropospheric Ozone From MAX-DOAS Measurements  
1076 During the CINDI-2 Campaign: Part 1—Development of a New Retrieval  
1077 Algorithm, *Journal of Geophysical Research: Atmospheres*, 123, 10,637-10,670,  
1078 <https://doi.org/10.1029/2018JD028647>, 2018.
- 1079 Wang, Y., Dörner, S., Donner, S., Böhnke, S., De Smedt, I., Dickerson, R. R., Dong,  
1080 Z., He, H., Li, Z., Li, Z., Li, D., Liu, D., Ren, X., Theys, N., Wang, Y., Wang, Y.,  
1081 Wang, Z., Xu, H., Xu, J., and Wagner, T.: Vertical profiles of NO<sub>2</sub>, SO<sub>2</sub>, HONO,  
1082 HCHO, CHOCHO and aerosols derived from MAX-DOAS measurements at a  
1083 rural site in the central western North China Plain and their relation to emission  
1084 sources and effects of regional transport, *Atmospheric Chemistry and Physics*, 19,  
1085 5417–5449, <https://doi.org/10.5194/acp-19-5417-2019>, 2019.
- 1086 Wang, Y., Gao, W., Wang, S., Song, T., Gong, Z., Ji, D., Wang, L., Liu, Z., Tang, G.,  
1087 Huo, Y., Tian, S., Li, J., Li, M., Yang, Y., Chu, B., Petäjä, T., Kerminen, V.-M.,  
1088 He, H., Hao, J., Kulmala, M., Wang, Y., and Zhang, Y.: Contrasting trends of  
1089 PM<sub>2.5</sub> and surface-ozone concentrations in China from 2013 to 2017, *Natl Sci  
1090 Rev*, 7, 1331–1339, <https://doi.org/10.1093/nsr/nwaa032>, 2020.
- 1091 Wang, Y., Yang, Y., Yuan, Q., Li, T., Zhou, Y., Zong, L., Wang, M., Xie, Z., Ho, H.  
1092 C., Gao, M., Tong, S., Lolli, S., and Zhang, L.: Substantially underestimated  
1093 global health risks of current ozone pollution, *Nat Commun*, 16, 102,  
1094 <https://doi.org/10.1038/s41467-024-55450-0>, 2025b.
- 1095 Wang, Z., Zhang, H., Shi, C., Ji, X., Zhu, Y., Xia, C., Sun, X., Zhang, M., Lin, X.,  
1096 Yan, S., Zhou, Y., Xing, C., Chen, Y., and Liu, C.: Vertical and spatial  
1097 differences in ozone formation sensitivities under different ozone pollution levels  
1098 in eastern Chinese cities, *npj Clim Atmos Sci*, 8, 30,  
1099 <https://doi.org/10.1038/s41612-024-00855-3>, 2025c.
- 1100 Xia, N., Du, E., Guo, Z., and de Vries, W.: The diurnal cycle of summer tropospheric  
1101 ozone concentrations across Chinese cities: Spatial patterns and main drivers,  
1102 *Environmental Pollution*, 286, 117547,  
1103 <https://doi.org/10.1016/j.envpol.2021.117547>, 2021.
- 1104 Xing, C., Liu, C., Wang, S., Chan, K. L., Gao, Y., Huang, X., Su, W., Zhang, C.,  
1105 Dong, Y., Fan, G., Zhang, T., Chen, Z., Hu, Q., Su, H., Xie, Z., and Liu, J.:  
1106 Observations of the vertical distributions of summertime atmospheric pollutants  
1107 and the corresponding ozone production in Shanghai, China, *Atmospheric  
1108 Chemistry and Physics*, 17, 14275–14289, [https://doi.org/10.5194/acp-17-14275-  
1109 2017](https://doi.org/10.5194/acp-17-14275-2017), 2017.
- 1110 Xing, C., Liu, C., Wang, S., Hu, Q., Liu, H., Tan, W., Zhang, W., Li, B., and Liu, J.:  
1111 A new method to determine the aerosol optical properties from multiple-

1112 wavelength O<sub>4</sub> absorptions by MAX-DOAS observation, *Atmospheric*  
1113 *Measurement Techniques*, 12, 3289–3302, [https://doi.org/10.5194/amt-12-3289-](https://doi.org/10.5194/amt-12-3289-2019)  
1114 2019, 2019.

1115 Xing, C., Liu, C., Wu, H., Lin, J., Wang, F., Wang, S., and Gao, M.: Ground-based  
1116 vertical profile observations of atmospheric composition on the Tibetan Plateau  
1117 (2017–2019), *Earth System Science Data*, 13, 4897–4912,  
1118 <https://doi.org/10.5194/essd-13-4897-2021>, 2021a.

1119 Xing, C., Liu, C., Hu, Q., Fu, Q., Wang, S., Lin, H., Zhu, Y., Wang, S., Wang, W.,  
1120 Javed, Z., Ji, X., and Liu, J.: Vertical distributions of wintertime atmospheric  
1121 nitrogenous compounds and the corresponding OH radicals production in Leshan,  
1122 southwest China, *Journal of Environmental Sciences*, 105, 44–55,  
1123 <https://doi.org/10.1016/j.jes.2020.11.019>, 2021b.

1124 Xing, C., Liu, C., Hong, Q., Liu, H., Wu, H., Lin, J., Song, Y., Chen, Y., Liu, T., Hu,  
1125 Q., Tan, W., and Lin, H.: Vertical distributions and potential sources of  
1126 wintertime atmospheric pollutants and the corresponding ozone production on  
1127 the coast of Bohai Sea, *Journal of Environmental Management*, 319, 115721,  
1128 <https://doi.org/10.1016/j.jenvman.2022.115721>, 2022.

1129 Xing, C., Xu, S., Song, Y., Liu, C., Liu, Y., Lu, K., Tan, W., Zhang, C., Hu, Q., Wang,  
1130 S., Wu, H., and Lin, H.: A new insight into the vertical differences in NO<sub>2</sub>  
1131 heterogeneous reaction to produce HONO over inland and marginal seas,  
1132 *Atmospheric Chemistry and Physics*, 23, 5815–5834,  
1133 <https://doi.org/10.5194/acp-23-5815-2023>, 2023.

1134 Xing, C., Liu, C., Li, Q., Wang, S., Tan, W., Zou, T., Wang, Z., and Lu, C.:  
1135 Observations of HONO and its precursors between urban and its surrounding  
1136 agricultural fields: The vertical transports, sources and contribution to OH,  
1137 *Science of The Total Environment*, 915, 169159,  
1138 <https://doi.org/10.1016/j.scitotenv.2023.169159>, 2024a.

1139 Xing, C., Liu, C., Ye, C., Xue, J., Wu, H., Ji, X., Ou, J., and Hu, Q.: Observations of  
1140 the vertical distributions of summertime atmospheric pollutants in Nam Co: OH  
1141 production and source analysis, *Atmospheric Chemistry and Physics*, 24, 10093–  
1142 10112, <https://doi.org/10.5194/acp-24-10093-2024>, 2024c.

1143 Xu, S., Wang, S., Xia, M., Lin, H., Xing, C., Ji, X., Su, W., Tan, W., Liu, C., and Hu,  
1144 Q.: Observations by Ground-Based MAX-DOAS of the Vertical Characters of  
1145 Winter Pollution and the Influencing Factors of HONO Generation in Shanghai,  
1146 China, *Remote Sensing*, 13, 3518, <https://doi.org/10.3390/rs13173518>, 2021.

1147 Xuan, H., Liu, J., Zhao, Y., Cao, Q., Chen, T., Wang, Y., Liu, Z., Sun, X., Li, H.,  
1148 Zhang, P., Chu, B., Ma, Q., and He, H.: Relative humidity driven nocturnal  
1149 HONO formation mechanism in autumn haze events of Beijing, *npj Clim Atmos*

- 1150 Sci, 7, 193, <https://doi.org/10.1038/s41612-024-00745-8>, 2024.
- 1151 Xuan, H., Lian, C., Ma, P., Lan, L., Wang, W., Liu, C., Quan, J., Zhang, S., Liu, J., Li,  
1152 H., Chen, T., Zhang, P., Wang, Y., Chu, B., Ma, Q., and He, H.: Vertical  
1153 Distribution of Sources and Atmospheric Impacts of HONO in the North China  
1154 Plain, *Environ. Sci. Technol.*, 59, 17666–17676,  
1155 <https://doi.org/10.1021/acs.est.5c01801>, 2025b.
- 1156 Xue, C., Ye, C., Zhang, C., Catoire, V., and Mu, Y.: Evidence for Strong HONO  
1157 Emission from Fertilized Agricultural Fields and its Remarkable Impact on  
1158 Regional O<sub>3</sub> Pollution in the Summer North China Plain, *ACS Earth and Space  
1159 Chemistry*, 5, <https://doi.org/10.1021/acsearthspacechem.0c00314>, 2021.
- 1160 Xue, C., Chen, H., McGillen, M. R., Su, H., Cheng, Y., Kleffmann, J., Li, G.,  
1161 Cazaunau, M., Colomb, A., Sciare, J., DeWitt, L., Marchand, N., Sarda-Estève,  
1162 R., Petit, J.-E., and Kukui, A.: Role of Heterogeneous Reactions in the  
1163 Atmospheric Oxidizing Capacity in Island Environments, *Environ. Sci. Technol.*,  
1164 59, 3153–3164, <https://doi.org/10.1021/acs.est.4c11647>, 2025.
- 1165 Yang, G., Liu, Y., and Li, X.: Spatiotemporal distribution of ground-level ozone in  
1166 China at a city level, *Sci Rep*, 10, 7229, <https://doi.org/10.1038/s41598-020-64111-3>, 2020.
- 1168 Ye, C., Lu, K., Ma, X., Qiu, W., Li, S., Yang, X., Xue, C., Zhai, T., Liu, Y., Li, X., Li,  
1169 Y., Wang, H., Tan, Z., Chen, X., Dong, H., Zeng, L., Hu, M., and Zhang, Y.:  
1170 HONO chemistry at a suburban site during the EXPLORE-YRD campaign in  
1171 2018: formation mechanisms and impacts on O<sub>3</sub> production, *Atmospheric  
1172 Chemistry and Physics*, 23, 15455–15472, <https://doi.org/10.5194/acp-23-15455-2023>, 2023a.
- 1174 Ye, C., Lu, K., Ma, X., Qiu, W., Li, S., Yang, X., Xue, C., Zhai, T., Liu, Y., Li, X., Li,  
1175 Y., Wang, H., Tan, Z., Chen, X., Dong, H., Zeng, L., Hu, M., and Zhang, Y.:  
1176 HONO chemistry at a suburban site during the EXPLORE-YRD campaign in  
1177 2018: formation mechanisms and impacts on O<sub>3</sub> production, *Atmospheric  
1178 Chemistry and Physics*, 23, 15455–15472, <https://doi.org/10.5194/acp-23-15455-2023>, 2023b.
- 1180 Yu, H., De Smedt, I., Theys, N., Snee, M., Veefkind, P., and Van Roozendaal, M.:  
1181 Harmonized cloud datasets for the Ozone Monitoring Instrument (OMI) and  
1182 TROPOspheric Monitoring Instrument (TROPOMI) using the O<sub>2</sub>–O<sub>2</sub>  
1183 477&thinsp;nm absorption band, *Atmospheric Measurement Techniques*, 18,  
1184 4131–4163, <https://doi.org/10.5194/amt-18-4131-2025>, 2025.
- 1185 Yu, Y., Cheng, P., Li, H., Yang, W., Han, B., Song, W., Hu, W., Wang, X., Yuan, B.,  
1186 Shao, M., Huang, Z., Li, Z., Zheng, J., Wang, H., and Yu, X.: Budget of nitrous  
1187 acid (HONO) at an urban site in the fall season of Guangzhou, China,

- 1188 Atmospheric Chemistry and Physics, 22, 8951–8971,  
1189 <https://doi.org/10.5194/acp-22-8951-2022>, 2022.
- 1190 Zeng, Y., Zhang, J., Li, D., Liao, Z., Bian, J., Bai, Z., Shi, H., Xuan, Y., Yao, Z., and  
1191 Chen, H.: Vertical distribution of tropospheric ozone and its sources of  
1192 precursors over Beijing: Results from ~ 20 years of ozonesonde measurements  
1193 based on clustering analysis, *Atmospheric Research*, 284, 106610,  
1194 <https://doi.org/10.1016/j.atmosres.2023.106610>, 2023.
- 1195 Zhang, H., Ren, C., Zhou, X., Tang, K., Liu, Y., Liu, T., Wang, J., Chi, X., Li, M., Li,  
1196 N., Huang, X., and Ding, A.: Improving HONO Simulations and Evaluating Its  
1197 Impacts on Secondary Pollution in the Yangtze River Delta Region, China,  
1198 *Journal of Geophysical Research: Atmospheres*, 129, e2024JD041052,  
1199 <https://doi.org/10.1029/2024JD041052>, 2024.
- 1200 Zhang, H., Shi, C., Ying, C., Weng, S., Ni, E., Zhao, L., Yang, P., Tang, K., Zhou, X.,  
1201 Ren, C., Chi, X., Zhou, D., Li, M., Li, N., Liu, T., and Huang, X.: HONO  
1202 formation mechanisms and impacts on ambient oxidants in coastal regions of  
1203 Fujian, China, *Atmospheric Chemistry and Physics*, 25, 16797–16816,  
1204 <https://doi.org/10.5194/acp-25-16797-2025>, 2025a.
- 1205 Zhang, Q., Liu, P., Wang, Y., George, C., Chen, T., Ma, S., Ren, Y., Mu, Y., Song,  
1206 M., Herrmann, H., Mellouki, A., Chen, J., Yue, Y., Zhao, X., Wang, S., and  
1207 Zeng, Y.: Unveiling the underestimated direct emissions of nitrous acid (HONO),  
1208 *Proc Natl Acad Sci U S A*, 120, e2302048120,  
1209 <https://doi.org/10.1073/pnas.2302048120>, 2023a.
- 1210 Zhang, X., Tong, S., Jia, C., Zhang, W., Wang, Z., Tang, G., Hu, B., Liu, Z., Wang,  
1211 L., Zhao, P., Pan, Y., and Ge, M.: Elucidating HONO formation mechanism and  
1212 its essential contribution to OH during haze events, *npj Clim Atmos Sci*, 6, 55,  
1213 <https://doi.org/10.1038/s41612-023-00371-w>, 2023b.
- 1214 Zhang, X., Yan, Y., Zhang, N., Wang, W., Suo, H., Jian, X., Wang, C., Ma, H., Gao,  
1215 H., Yang, Z., Huang, T., and Ma, J.: The 21st-century wetting inhibits growing  
1216 surface ozone in Northwestern China, *Atmospheric Chemistry and Physics*, 25,  
1217 9669–9684, <https://doi.org/10.5194/acp-25-9669-2025>, 2025b.
- 1218 Zhang, Y., Zhang, Y., Liu, Z., Bi, S., and Zheng, Y.: Analysis of Vertical Distribution  
1219 Changes and Influencing Factors of Tropospheric Ozone in China from 2005 to  
1220 2020 Based on Multi-Source Data, *International Journal of Environmental  
1221 Research and Public Health*, 19, 12653, <https://doi.org/10.3390/ijerph191912653>,  
1222 2022.
- 1223 Zhou, M., Li, Y., and Zhang, F.: Spatiotemporal Variation in Ground Level Ozone  
1224 and Its Driving Factors: A Comparative Study of Coastal and Inland Cities in  
1225 Eastern China, *International Journal of Environmental Research and Public*

- 1226 Health, 19, 9687, <https://doi.org/10.3390/ijerph19159687>, 2022.
- 1227 Zhu, L., Wang, J., Xu, Y., Ma, N., Song, X., Qin, J., Li, B., Tsui, W. B. C., Lv, L.,  
1228 and Zhang, T.: Vertical Characteristics of an Ozone Pollution Episode in Hong  
1229 Kong Under the Typhoon Mawar—A Case Study, *Remote Sensing*, 17, 3904,  
1230 <https://doi.org/10.3390/rs17233904>, 2025a.
- 1231 Zhu, X., Wang, H., Han, Y., Zhang, D., Liu, S., Zhang, Z., and Liu, Y.:  
1232 Reconstructing the VOC–Ozone Research Framework Through a Systematic  
1233 Review of Observation and Modeling, *Sustainability*, 17, 7512,  
1234 <https://doi.org/10.3390/su17167512>, 2025b.
- 1235 Zou, T., Xing, C., Xue, J., Li, Q., Tan, W., Wu, Z., and Liu, C.: Transport  
1236 characteristics of urban and rural aerosols based on vertical observations and  
1237 deep learning predictions, *Atmospheric Research*, 315, 107876,  
1238 <https://doi.org/10.1016/j.atmosres.2024.107876>, 2025.